

## ORIGINAL ARTICLE

# Simvastatin overcomes the pPCK1-pLDHA-SPRINGlac axis-mediated ferroptosis and chemo-immunotherapy resistance in AKT-hyperactivated intrahepatic cholangiocarcinoma

Jinghan Zhu<sup>1,2</sup>  | Yixiao Xiong<sup>1,2,3</sup> | Yuxin Zhang<sup>1,2,4</sup> | Huifang Liang<sup>1,2,5</sup>  | Kun Cheng<sup>1,2</sup> | Yuanxiang Lu<sup>1,2</sup> | Guangzhen Cai<sup>1,2</sup> | Yang Wu<sup>1,2</sup> | Yunhui Fan<sup>1,2</sup> | Xiaoping Chen<sup>1,2,5</sup> | Hong Zhu<sup>6</sup> | Zeyang Ding<sup>1,2,5</sup> | Wanguang Zhang<sup>1,2,5</sup> 

**List of Abbreviations:** 2-DG, 2-deoxyglucose; 2-NBDG, 2-(n-(7-nitrobenz-2-oxa-1,3-diazol-4-yl) amino)-2-deoxyglucose; ABCA1, ATP-binding cassette subfamily A member 1; ABCG1, ATP-binding cassette subfamily G member 1; ACACA, acetyl-CoA carboxylase alpha; AKT, protein kinase B; CAR-T, chimeric antigen receptor T cells; CIP, calf intestinal phosphatase; Cis, cisplatin; CIT, chemo-immunotherapy (gemcitabine + cisplatin + anti-PD-L1); CK19, cytokeratin 19; CoA, coenzyme A; Con, control; CoQ<sub>2</sub>, coenzyme Q2 polyprenyltransferase; Cre, cre recombinase; CRISPR, clustered regularly interspaced short palindromic repeats; DCR, disease control rate; DFO, deferoxamine; DHCR24, 24-dehydrocholesterol reductase; DHCR7, 7-dehydrocholesterol reductase; ECAR, extracellular acidification rate; ECC, extrahepatic cholangiocarcinoma; ERK1/2, extracellular signal-regulated kinase 1/2; ERP72, endoplasmic reticulum protein 72; FASN, fatty acid synthase; FDFT1, farnesyl-diphosphate farnesyltransferase 1 (Squalene synthase); FDPS, farnesyl diphosphate synthase; FFA, free fatty acids; FPP, farnesyl pyrophosphate; FSP1, ferroptosis suppressor protein 1; gDNA, genome DNA; GDP, guanosine diphosphate; Gem, gemcitabine; GGPP, geranylgeranyl pyrophosphate; GM130, golgi matrix protein of 130 kDa; GP, gemcitabine + cisplatin; GPAM, glycerol-3-phosphate acyltransferase mitochondrial; GPX4, glutathione peroxidase 4; GSH, glutathione; GTP, guanosine triphosphate; H&E, hematoxylin and eosin staining; hHER2, human epidermal growth factor receptor 2; HMG-CoA, 3-hydroxy-3-methylglutaryl-coenzyme A; HMGCR, 3-hydroxy-3-methylglutaryl-CoA reductase; HMGCS1, 3-hydroxy-3-methylglutaryl-CoA synthase 1; HNF4A, hepatocyte nuclear factor 4 alpha; IC50, half maximal inhibitory concentration; ICC, intrahepatic cholangiocarcinoma; ID1I, isopentenyl-diphosphate delta isomerase 1; IFN $\gamma$ , interferon gamma; IGF-1, insulin growth factor 1; IKE, imidazole ketone erastin; INSIG1/2, insulin-induced gene 1/2; IP-MS, immunoprecipitation followed by mass spectrometry; KO, knockout; KP, Kras<sup>G12D</sup>+Tp53<sup>-/-</sup>; Kras, kirsten rat sarcoma viral oncogene; LDHA, lactate dehydrogenase A; LDLR, low-density lipoprotein receptor; Lip1, lipoxstatin-1; LSS, lanosterol synthase; MAGECK, model-based analysis of genome-wide CRISPR-Cas9 knockout; MDA, malondialdehyde; MK4, menaquinone-4; mRECIST 1.1, modified response evaluation criteria in solid tumors version 1.1; MUFA, monounsaturated fatty acid; MVA, mevalonate; MVA-Li, mevalonic acid lithium salt; MVD, mevalonate diphosphate decarboxylase; MVK, mevalonate kinase; Nala, sodium L-lactate; Nec-1, necrostatin-1s; NGS, next-generation sequencing; NSDHL, NAD(P)H steroid dehydrogenase-like; ORR, overall response rate; OS, overall survival; OVA, ovalbumin; pAKT, phosphorylated AKT (pS473); pan-Kac, pan-lysine-acetylation; pan-Klac, pan-lysine lactylation; PCK1, phosphoenolpyruvate carboxykinase 1; PD-L1, programmed death-ligand 1; PDO, patient-derived organoid; PEP, phosphoenolpyruvate; PLs, phospholipids; PPB, PCK1 phosphorylation blocker; pPCK1, phosphorylated PCK1 (pS90); PR, partial response; PTEN, phosphatase and tensin homolog; PUFA, polyunsaturated fatty acid; Pyruvate-Na, sodium pyruvate; Rot/AA, rotenone/antimycin A; rPCK1, PCK1-KO +recombinant PCK1 overexpression; RT-qPCR, reverse transcription quantitative polymerase chain reaction; SC4MOL, sterol-C4-methyl oxidase-like; SCAP, SREBP cleavage-activating protein; SCD1, stearoyl-CoA desaturase 1; Scr, scramble shRNA; scRNA, single-cell RNA sequencing; sgRNA, single-guide RNA; shRNA, short hairpin RNA; Simv, simvastatin; Sox9, SRY-Box transcription factor 9; SPRING, SREBP-regulating gene protein; SQLE, squalene epoxidase; SRE, sterol regulatory element; SREBP1/2, sterol regulatory element-binding protein 1/2; TAT, trans-activator of transcription; TMA, tissue microarray; TNF $\alpha$ , tumor necrosis factor alpha; Tp53, tumor protein 53; UBIAD1, ubiA prenyltransferase domain-containing protein 1; UMAP, uniform manifold approximation and projection; WT, wild type; Z-V, Z-VAD-FMK.

† Jinghan Zhu, Yixiao Xiong, Yuxin Zhang and Huifang Liang have contributed equally to this work.

This is an open access article under the terms of the [Creative Commons Attribution-NonCommercial-NoDerivs](https://creativecommons.org/licenses/by-nc-nd/4.0/) License, which permits use and distribution in any medium, provided the original work is properly cited, the use is non-commercial and no modifications or adaptations are made.

© 2025 The Author(s). *Cancer Communications* published by John Wiley & Sons Australia, Ltd. on behalf of Sun Yat-sen University Cancer Center.

## Correspondence

Wanguang Zhang, Zeyang Ding and Xiaoping Chen, Hepatic Surgery Center, Tongji Hospital, Tongji Medical College, Huazhong University of Science and Technology, Wuhan, Hubei, P. R. China. Email: [wgzhang@tjh.tjmu.edu.cn](mailto:wgzhang@tjh.tjmu.edu.cn), [zyding@tjh.tjmu.edu.cn](mailto:zyding@tjh.tjmu.edu.cn) and [chenxpchenxp@163.com](mailto:chenxpchenxp@163.com)

Hong Zhu, Department of Medical Oncology, the First Affiliated Hospital of Soochow University, Suzhou, Jiangsu, P. R. China. Email: [zhuhong\\_jasmine@suda.edu.cn](mailto:zhuhong_jasmine@suda.edu.cn)

## Funding information

National Natural Science Foundation of China, Grant/Award Numbers: 81874149, 82171834, 82303832, 82403618; China Postdoctoral Science Foundation, Grant/Award Number: 2024M761039; China National Postdoctoral Program for Innovative Talents, Grant/Award Number: BX20240129; Postdoctor Project of Hubei Province, Grant/Award Number: 2024HBBHCXA035; Knowledge Innovation Program of Wuhan-Shuguang Project, Grant/Award Number: 2022020801020456; Key Research and Development Program of Social Development of Jiangsu Province, Grant/Award Number: BE2022725; Suzhou Science and Technology Development Plan Project, Grant/Award Number: SKY2023049; Jiangsu Province Seventh 333 High Level (Second Level) Talents Project

## Abstract

**Background:** Intrahepatic cholangiocarcinoma (ICC) is a challenging cancer with an increasing incidence. The Phase III TOPAZ-1/KEYNOTE-966 study demonstrated chemo-immunotherapy (CIT) as a significant advancement, potentially replacing traditional chemotherapy for advanced biliary tract cancer. Ferroptosis is a crucial process that affects cancer cell survival and therapy resistance. Although AKT hyperactivation is prevalent in numerous cancers, including ICC, its role in ferroptosis resistance remains unclear. This study explored whether targeting ferroptosis can enhance CIT response rates, specifically in ICC patients with AKT hyperactivation.

**Methods:** In vivo metabolic CRISPR screening in a  $Kras^{G12D}/Tp53^{-/-}$  ICC mouse model was used to identify primary regulators of ferroptosis during CIT (gemcitabine, cisplatin, and anti-mouse programmed cell death 1 ligand 1). Phosphoenolpyruvate carboxykinase 1 (PCK1) was assessed for its role in ferroptosis and treatment resistance in preclinical models under AKT activation levels. Molecular and biochemical techniques were used to explore PCK1-related resistance mechanisms in AKT-hyperactivated ICC.

**Results:** Under AKT hyperactivation condition, phosphorylated PCK1 (pPCK1) promoted metabolic reprogramming, enhancing ubiquinol and menaquinone-4 synthesis through the mevalonate (MVA) pathway. This cascade was mediated by the pPCK1-pLDHA-SPRINGlac axis. Inhibiting PCK1 phosphorylation or using simvastatin significantly augmented CIT efficacy in preclinical models. Clinical data further indicated that phosphorylated AKT (pAKT)-pPCK1 levels might serve as a biomarker to predict CIT response in ICC.

**Conclusion:** This study identified the pAKT-pPCK1-pLDHA-SPRINGlac axis as a novel mechanism driving ferroptosis resistance in AKT-hyperactivated ICC by associating glycolytic activation with MVA flux reprogramming. Targeting this axis, potentially through statin-based therapies, may offer a strategy to sensitize ICC cells to ferroptosis and improve treatment outcomes.

## KEYWORDS

Chemo-immunotherapy, Ferroptosis, Intrahepatic cholangiocarcinoma, Lactylation, Mevalonate pathway, PCK1

## 1 | BACKGROUND

Intrahepatic cholangiocarcinoma (ICC) is a highly aggressive malignancy with chemotherapy resistance, immune evasion, and a poor 5-year survival rate of less than 20% [1, 2]. Although a chemo-immunotherapy (CIT) regimen combining gemcitabine, cisplatin, and durvalumab has shown modest success [3], persistent resistance and low response rates underscore the urgent need for novel therapeutic strategies.

Resistance to chemotherapy and immunotherapy in ICC may fundamentally arise from its unique metabolic features [4]. ICC is characterized by aerobic glycoly-

sis and lipid metabolism reprogramming, both closely linked to ferroptosis [5–7], suggesting that ferroptosis may play a critical role in the initiation, progression, and treatment resistance of ICC. Although chemotherapy primarily induces tumor cell apoptosis, apoptosis alone cannot fully explain the additive sensitization observed with combined chemotherapy and immunotherapy. Instead, chemotherapy and immunotherapy-induced immunogenic cell death, such as ferroptosis and necroptosis, is increasingly recognized as the underlying mechanism driving this effect [8]. However, the role of ferroptosis in ICC, particularly its association with chemotherapy and immunotherapy resistance, remains poorly understood.

Although lipid metabolism reprogramming is associated with tumor progression, its impact on ferroptosis remains complex. Two major transcription factors in lipid metabolism, sterol regulatory element-binding protein 1 (SREBP1) and sterol regulatory element-binding protein 2 (SREBP2), play distinct roles in regulating fatty acid and cholesterol metabolism, respectively. SREBP1 downstream target acyl-coenzyme A (acyl-CoA) synthetase long-chain family member 4 promotes polyunsaturated fatty acid (PUFA) synthesis, sensitizing cells to lipid peroxidation [9, 10]. However, activation of the phosphatidylinositol 3-kinase (PI3K)-protein kinase B (AKT)-mechanistic Target of Rapamycin (mTOR) pathway enhances monounsaturated fatty acid (MUFA) synthesis by upregulating stearoyl-CoA desaturase 1 (SCD1) via SREBP1, thereby conferring ferroptosis resistance to tumor cells [11]. Meanwhile, SREBP2-driven transcription of transferrin has been implicated in ferroptosis resistance in melanoma cells [12], while cholesterol metabolism is a primary source of reduced coenzyme Q<sub>10</sub> (CoQ<sub>10</sub>H<sub>2</sub>) and menaquinone-4 (MK4), both of which serve as key radical-trapping antioxidants that enhancing cells' ferroptosis surveillance ability. In ICC, understanding the relationship among fatty acid metabolism, cholesterol metabolism, and ferroptosis resistance is critical for developing novel therapeutic strategies to improve patient outcomes [13].

In this study, we hypothesized that ferroptosis plays a central role in CIT resistance in ICC, driven by intricate metabolic reprogramming. To test this hypothesis, we performed a metabolic CRISPR screen in an *in vivo* murine ICC model, and identified key ferroptosis modulators with the potential to enhance CIT efficacy. Molecular and biochemical analyses revealed that phosphorylated PCK1 (pPCK1)-mediated glycolytic activation and mevalonate (MVA) flux reprogramming are critical mechanisms driving ferroptosis and CIT resistance in AKT-hyperactivated ICC. Importantly, simvastatin treatment effectively reversed this resistance, underscoring its therapeutic potential in improving CIT efficacy.

## 2 | Materials and Methods

### 2.1 | The construction of the murine KP-ICC cell line

Using the *Kras*<sup>G12D</sup>+*Tp53*<sup>flox/flox</sup> genetically engineered mouse model, hepatocyte-specific Cre expression drives spontaneous tumorigenesis leading to ICC development [14]. Based on this model, we established 2 murine ICC cell line, KP-ICC and KP2, derived from tumors arising in this context. Briefly, male *Kras*<sup>G12D</sup>+*Tp53*<sup>flox/flox</sup> C57BL/6J (4–5 weeks old), provided by Bo Zhong (Wuhan University,

Wuhan, Hubei, China), were subjected to hydrodynamic tail vein injection. A plasmid mixture (2 mL saline), containing 20 µg pT3-Cre and 2.4 µg sleeping beauty transposase plasmids, was rapidly injected into the liver via the tail vein within 7 s.

Tumors were harvested 6 months post-injection. The derived tumor cells were isolated and cultivated under 2D monolayer culture and 3D organoid culture (details about organoid culture are provided in the “**Patient-derived organoid construction and culture conditions**” subsection). For the 2D culture, primary tumor cells were cultured in RPMI 1640 medium supplemented with 10% fetal bovine serum (FBS), 1× penicillin/ streptomycin (MA0110, Meilunbio, Dalian, Liaoning, China). After 5 passages, these cells underwent single-cell clone selection by serial dilution. Cells were diluted to 1 cell per well in 96-well plates and incubated at 37°C with 5% CO<sub>2</sub> for 2 weeks.

Post-selection, clones successfully integrated with Cre [verified by reverse transcription quantitative PCR (RT-qPCR)] were subjected to subsequent assays. The validation tests included the evaluation of p53 expression, examination of the activation status of both mitogen-activated protein kinase (MAPK) and AKT pathways [AKT, AKT pS473, extracellular signal-regulated kinase 1/2 (ERK1/2), ERK1/2 pT202/pY204], short tandem repeat (STR) identification (Supplementary Table S1), tumorigenicity assessment, and immunohistochemical (IHC) analysis of hepatocyte nuclear factor 4 alpha (HNF4A), cytokeratin 19 (CK19), and SRY-box transcription factor 9 (SOX9) in subcutaneous tumors.

In this study, two cell lines exhibiting ICC phenotypes, KP1 and KP2, were successfully established. Among them, KP1 was designated as KP-ICC and selected as the primary mouse-derived ICC cell line for subsequent experiments.

### 2.2 | Patient-derived organoid (PDO) construction and culture conditions

Human ICC tissues were collected from 10 treatment-naïve patients diagnosed based on imaging and clinical findings between December 2021 and July 2022 at the Hepatic Surgery Center, Tongji Hospital, Huazhong University of Science and Technology (Wuhan, Hubei, China). Final validation of ICC identity integrated clinical-pathological reports with CK19 immunostaining of the established PDOs. The study was approved by the institutional review board of Tongji Hospital (TJ-IRB20230112). All research procedures adhered to the principles set forth in the declaration of Helsinki and the declaration of Istanbul. Clinical and pathological characteristics of the patients are summarized in Supplementary Table S2.

ICC-PDOs were established as described previously [15]. Briefly, fresh tumor samples were collected and immediately stored in a preservation solution consisting of Advanced Dulbecco's Modified Eagle's Medium (DMEM)/F12 (#12634028, Gibco, Waltham, MA, USA) with 1% 4-(2-Hydroxyethyl)-1-piperazineethanesulfonic acid (HEPES) (S6831, Selleck-Chem, Houston, TX, USA), 1% GlutaMax (#35050061, Gibco), 1× penicillin/ streptomycin, and 10 µmol/L Y27632 (TB1254, R&D Systems, Minneapolis, MN, USA) until digestion (within 2 h). For tissue digestion, tumor specimens (0.5-1.5 cm<sup>3</sup>) were minced and digested in 5 mL of digestion buffer at 37°C. The digestion buffer consisted of the preservation solution supplemented with 4 mg/mL collagenase D (BS165, Biosharp, Hefei, Anhui, China), 1 mg/mL Dispase II (#04942078001, Sigma-Aldrich, St. Louis, MO, USA), 0.1 mg/mL DNase I (D8071, Solarbio, Beijing, China), and 100 µg/mL Primocin (ant-pm-1, InvivoGen, San Diego, CA, USA). Digestion was monitored microscopically every 5 min until single-cell clusters were observed. The digestion mixture was then filtered through a 70 µm nylon cell strainer. The resulting pellet was washed twice with cold Advanced DMEM/F12, and resuspended in organoid culture medium composed of Advanced DMEM/F12, 1× penicillin/streptomycin, 1% GlutaMax, 1% HEPES, 100 µg/mL Primocin, 50× B27 supplement (#12587010, Gibco), 1.25 mmol/L N-acetyl-L-cysteine (A9165, Sigma-Aldrich), 50 ng/mL recombinant human epidermal growth factor (EGF) (AF-100-15, Peprotech, Cranbury, NJ, USA), 100 ng/mL recombinant human fibroblast growth factor 10 (FGF10) (345-FG, R&D Systems), 1 ng/mL recombinant human fibroblast growth factor-basic (FGF-basic) (233-FB, R&D Systems), 25 ng/mL recombinant human hepatocyte growth factor (HGF) (100-39H, Peprotech), 10 µmol/L forskolin (#1099, Sigma-Aldrich), 5 µmol/L A8301 (#2939, R&D Systems), 10 µmol/L Y27632 (used in the first 3 days of culture) (TB1254, R&D Systems), 10 mmol/L nicotinamide (N0636, Sigma-Aldrich), 3 nmol/L dexamethasone (D1756, Sigma-Aldrich), 10 nmol/L gastrin (#3006, R&D Systems), 1 µmol/L SB202190 (#1264, R&D Systems), 1 µmol/L prostaglandin E2 (PGE2) (#2296, R&D Systems), 1 µmol/L chiron 99021 (CHIR 99021) (#4423, Tocris, Bristol, UK), 250 ng/mL recombinant human R-spondin-1 (CX83, Novoprotein, Shanghai, China), 30 ng/mL recombinant human Wnt3a (C18K, Novoprotein), and 30 ng/mL recombinant human Noggin (#6057-NG, R&D Systems). A 10 µL aliquot of the cell suspension was mixed with 25 µL Reduced growth factor-basement membrane extract (RGF-BME) (#3536, Bio-Techne, Minneapolis, MN, USA), and cultured in a 48-well suspension culture plate (#353047, Corning Incorporated, Corning, NY, USA) at 37°C for 1 h. After gelation, 300 µL of organoid culture medium was added

to each well. Established PDOs were dissociated to single cells with TrypLE (#12604013, Gibco) for 5 min at 37°C and passage into fresh medium and matrix every week. The success rate of PDO establishment from tumor tissue was approximately 50%, which can be further improved. It typically takes 4-6 weeks to achieve stable organoid expansion for subsequent studies. PDOs between passages 5 and 30 were used for experiments.

### 2.3 | Cell lines and cell culture conditions

Human ICC cell lines HuCCT-1, RBE, HuH-28 and human embryonic kidney cell line HEK-293T were obtained from the Shanghai Cell Bank of the Chinese Academy of Sciences (Shanghai, China). Human extrahepatic cholangiocarcinoma (ECC) cell line TFK-1, human ICC cell lines CCLP-1 and HCCC-9810 cell lines were gifts from Liwei Dong (Naval Medical University, Shanghai, China); human ECC cell line SK-ChA-1, MZ-ChA-1, and human ICC cell line QBC939 were kindly supplied by Chundong Yu (Xiamen University, Xiamen, Fujian, China). Human ICC cell lines EGI-1 cell lines were provided by Jianming Wang (Huazhong University of Science and Technology). All aforementioned cell lines are human ICC or ECC cell lines and were subjected to STR identification prior to the commencement of experiments.

All human ICC/ECC cell lines and murine KP-ICC cells were cultured in RPMI 1640 medium supplemented with 10% FBS, 1× penicillin/ streptomycin. The HEK-293T cell line was maintained in DMEM with 10% FBS, 1× penicillin/streptomycin. All cell lines were incubated at 37°C in a humidified atmosphere with 5% CO<sub>2</sub>.

### 2.4 | Genetic and transcriptomic similarities analyses

Two replicate samples from KP-ICC cells were collected and stored in Trizol (15596018CN, Invitrogen, Carlsbad, CA, USA) at -80°C. DNA and RNA was co-extracted using FastPure DNA/RNA Mini Kit V2 (RC313, Vazyme, Nanjing, Jiangsu, China), and submitted to GenePlus Technology (Beijing, China) for whole-exome sequencing (WES) and transcriptome sequencing. The WES library was prepared using the VAHTS Universal Plus DNA Library Prep Kit for MGI V2 (NDM627, Vazyme), while the transcriptome library was prepared using the VAHTS Universal V10 RNA-seq Library Prep Kit (NRM606, Vazyme). Following library preparation, sequencing was performed on the MGISEQ-2000 platform (MGI Tech, Shenzhen, Guangdong, China) with dual indexing.

For tumor mutation analysis, the raw reads of WES data of the KP-ICC (this work) and KPPC (PRJNA1066342), a recently reported ICC cell line derived from the same *Kras*<sup>G12D</sup>+*Tp53*<sup>-/-</sup> mouse model [16], were aligned to the mouse reference genome (GRCm39) using STAR v2.7 [17], followed by duplicate removal with Picard v2.27 (Broad Institute, Cambridge, MA, USA), base quality recalibration with GATK v4.2.6 (Broad Institute), and variant calling with GATK-Mutect2 module (GATK v4.2.6, Broad Institute). Tumor mutation burden (TMB) values were then calculated based on the number of nonsynonymous mutations per megabase of coding sequence.

For transcriptomic similarities analysis, raw reads of transcriptome data from the KP-ICC and KPPC models were aligned to the mouse reference genome (GRCm39) using STAR v2.7.9, and gene counts were extracted using FeatureCounts from the Subread package v2.0.3 [18]. Normalization of gene counts was performed using limma v3.52.4 [19], and batch effects were corrected using ComBat-seq from the sva package v3.40 [20]. Transcriptomic similarities were calculated using Spearman correlation coefficients ( $\rho$ ) across the normalized expression profiles.

## 2.5 | Viral library production and transduction

Mouse CRISPR Metabolic Gene Knockout library (#160129, Addgene, Watertown, MA, USA) targeting 2,865 mouse metabolic genes, including most metabolic enzymes and transporters [21], was a gift from Kivanc Birsoy (The Rockefeller University, New York, NY, USA). The CRISPR library plasmids were validated by next-generation sequencing (NGS) before conducting in vivo and in vitro CRISPR screening, the sequence data had been deposited in the National Genomics Data Center under accession number PRJCA020671. For the formal CRISPR screening, the library plasmids were transfected into HEK-293T cells at 90% confluence in 15 cm tissue culture plates. Viral supernatant was collected at 48 h and 72 h post-transfection, filtered via a 0.45 mm filtration unit. The supernatant was subsequently concentrated using polyethylene glycol 8000 (PEG8000) (25322-68-3, Dingguo Bio, Beijing, China) and stored in -80°C freezer until use.

For the viral transduction of KP-ICC cells, cells were subjected to lentiviral transduction with the CRISPR library at a Multiplicity of Infection (MOI) of 0.3. After a 3-day selection with puromycin, roughly 30% of the cells were set aside as Day 0-input controls. The remaining cells were then allocated for subsequent in vitro or in vivo screening assays.

## 2.6 | CRISPR-based screening

For in vivo screening, the details are described in the “**Mouse model**” subsection. For in vitro screening, lentivirus-infected KP-ICC cells were seeded at a density of  $1 \times 10^7$  cells per 15 cm dish (3 dishes per group) and treated with or without 10  $\mu\text{mol/L}$  (1S,3R)-RSL3 (RSL3) (S8155, Selleck-Chem), a commonly used ferroptosis inducer, for 36 h.

Tumors or cells were harvested post-screening, and genomic DNA was extracted as previously described [22]. Briefly, frozen tumors or cells were mechanically disrupted and lysed in lysis buffer [400 mmol/L NaCl, 10 mmol/L Tris-HCl, 2 mmol/L ethylenediaminetetraacetic acid (EDTA), 0.5% sodium dodecyl sulfate (SDS), pH 8.0]. Lysates were incubated with Proteinase K (50  $\mu\text{g/mL}$ , 4333793, Invitrogen) and RNase A (10  $\mu\text{g/mL}$ , EN0531, Invitrogen) at 56°C for 3 h, followed by phenol/chloroform extraction to remove proteins. Genomic DNA was precipitated, washed, and resuspended in nuclease-free water. DNA concentration was measured using a Nanodrop spectrophotometer (Thermo Scientific, Waltham, MA, USA).

Then, the DNA were subjected for library construction and sequencing. Genomic DNA from 5 tumors was pooled into 1 sample for library construction. A 2-step PCR strategy was employed to amplify the sgRNA cassette region for sequencing. The first PCR reaction amplified the sgRNA cassette region using sgRNA-specific primers (sgRNA-Forward: 5'-ATTTCTTGGGTAGTTTGCAGTTT-3'; sgRNA-Reverse: 5'-GACTCGGTG CCACTTTTTC-3'), and the second PCR reaction introduced sequencing adapters (Adaptor-Forward: 5'-TCGTCGGCAGCGTCAG ATGTGTATAAGAGACAG-3'; Adaptor-Reverse: 5'-GTCT CGTGGGCTCGGAGATGTGTATAAGAGACG-3'). Each PCR reaction contained 25  $\mu\text{L}$  HiFi amplification mix (N616, Vazyme), 2.5  $\mu\text{L}$  forward primer, 2.5  $\mu\text{L}$  reverse primer, 10  $\mu\text{g}$  template DNA or 5  $\mu\text{g}$  PCR products (for the second round), and nuclease-free water to a final volume of 50  $\mu\text{L}$ . PCR cycling conditions were 98°C for 45 s, followed by 25 cycles of 98°C for 15 s, 60°C for 30 s, and 72°C for 30 s, with a final extension at 72°C for 1 min. Post-amplification, 200-300 bp PCR products were gel-purified, and their concentration was determined using a Qubit fluorometer (Thermo Scientific). Normalized samples were pooled with 10%-20% Enterobacteria phage  $\phi\text{X174}$  (PhiX) and sequenced on a HiSeq 2500 system (Illumina, San Diego, CA, USA).

Sequencing data were processed utilizing the MAGeCK software [23]. Specifically, the MAGeCK-Maximum Likelihood Estimation module was employed to assess the sgRNA abundance variations between treatment and control groups. In the context of in vivo screening, the gene depletion or enrichment under treatments with GP,

anti-PD-L1, and CIT was normalized relative to the placebo group. For *in vitro* screening analysis, changes in target gene expression under RSL3 treatment were normalized against the dimethyl sulfoxide (DMSO) control group. Genes exhibiting significant depletion or enrichment were identified with a Wald *P*-value threshold of less than 0.05.

We categorized genes with a  $\beta$ -score ratio surpassing 1.5 when compared between CIT and either GP monotherapy or anti-PD-L1 monotherapy as potential synergistic mediators for CIT ( $\beta$ -score ratio =  $\frac{\beta \text{ score of Gene } x \text{ in CIT group}}{\beta \text{ score of Gene } x \text{ in GP/PD-L1 group}}$ ). This criterion was applied to pinpoint genes that demonstrated a marked increase in effect size upon the combination of CIT with other therapeutic modalities, as opposed to single-agent treatments.

## 2.7 | Mouse model

The implementation of all animal studies adhered to stringent guidelines, approved by the Institutional Animal Care and Use Committee of Tongji Hospital, affiliated with Huazhong University of Science and Technology. The studies followed the Animal Research: Reporting of *in vivo* Experiments guidelines [24] and conformed to the USA National Institutes of Health's guide for the care and use of laboratory animals [25], ensuring the humane treatment of all animals involved. Humane endpoints included severe weight loss ( $\geq 20\%$  of baseline body weight), impaired mobility (inability to access food or water), or signs of distress (hunched posture, labored breathing, or self-mutilation). Euthanasia was performed using CO<sub>2</sub> inhalation at a concentration of 70% followed by cervical dislocation to ensure a humane and ethical process.

All animals were housed under specific pathogen-free conditions to maintain the integrity of the experiments. The allocation of animals to various treatment cohorts was meticulously randomized, utilizing multiple strategies to diminish potential selection bias. This included the use of littermates to assign animals randomly across different groups, random integration of mice prior to treatment (assuring even distribution from various cages in each group), and/or random assignment of mice to each group, with careful consideration to factors such as gender, age variance, cage, and housing position, wherever pertinent. All these measures were taken to guarantee the robustness and validity of the results. Furthermore, to control selection bias, the average tumor sizes were consistent across different treatment groups at the initiation of treatments.

For tumorigenicity assessment of KP-ICC,  $2 \times 10^6$  cells were subcutaneously injected into 5-6 weeks old male C57BL/6J mice. One-week post-injection, the subcutaneous tumors were harvested for subsequent analyses. For

the KP-ICC subcutaneous model,  $1 \times 10^6$  KP-ICC cells were injected subcutaneously into 5-6 weeks old male C57BL/6J mice or BALB/c nude mice (GemPharmatech, Nanjing, Jiangsu, China).

For *in vivo* screening, lentivirus-infected KP-ICC cells ( $5 \times 10^6$ , at approximately 500-fold sgRNA coverage) were injected subcutaneously into the flanks of 4- to 5-week-old C57BL/6J mice in 100  $\mu$ L of 40% Matrigel (354248, Corning). Tumors were allowed to grow for 1 week, during which mice were treated daily with 10 mg/kg liproxstatin-1 (Lip1, S7699, Selleck-Chem) intraperitoneally to prevent the loss of ferroptosis-related genes before treatment initiation.

For the hydrodynamic tail vein injection-induced ICC mouse model, 4-5 weeks old male C57BL/6J mice received a hydrodynamic tail vein injection. The injection consisted of a plasmid mixture dissolved in 2 mL of saline, containing 20  $\mu$ g pT3-myr-Akt-IRES-luciferase (a gift from Furong Liu, Huazhong University of Science and Technology [26]), 20  $\mu$ g pT3-NICD (#46047, Addgene), and 2.4  $\mu$ g sleeping beauty transposase plasmids (#34879, Addgene). This 2 mL mixture was rapidly delivered to the liver via the tail vein within approximately 7 s.

## 2.8 | Drug treatments in mouse models

At 1 week after tumor cell injection for the KP-ICC subcutaneous model and 2 weeks after injection for the hydrodynamic tail vein injection-induced ICC model, mice were initiated on a 5-cycle treatment regimen. The regimens included placebo, GP (gemcitabine + cisplatin), anti-PD-L1, and CIT. For the placebo group, an isotype control of rat IgG2b (LTF-2, A2116, Selleck Chem) was administered at a dose of 10 mg/kg. The GP regimen consisted of intraperitoneal injection of 30 mg/kg gemcitabine (HY-17026, MedChemExpress, Monmouth Junction, NJ, USA) and 3 mg/kg cisplatin (S1166, Selleck Chem). The anti-PD-L1 treatment involved the intraperitoneal injection of 10 mg/kg anti-mouse PD-L1 (anti-mPD-L1) antibody (10F.9G2, A2115, Selleck Chem). In the CIT group, mice received chemotherapy with gemcitabine and cisplatin on Day 1 and an intraperitoneal injection of the anti-mPD-L1 antibody on Day 2, and rested with no treatment on Day 3. This 3-day cycle was repeated for a total of 5 cycles, with 1-day intervals between cycles 1-2 and 3-4, and 2-day intervals between cycles 2-3 and 4-5.

In the *in vivo* rescue assays, in addition to the 4 aforementioned foundational treatments, 40 mg/kg PCK1 phosphorylation blocker (PPB peptide) (DVARIESKTVI, custom-designed by our team, synthesized by ChinaPeptides, Shanghai, China) was injected intraperitoneally every 2 days to inhibit PCK1 pS90; 5 mg/kg simvastatin

(S1792, Selleck Chem) was administered intragastrically via gavage every 2 days to inhibit the MVA pathway; 10 mg/kg Lip1 was injected intraperitoneally every day to inhibit ferroptosis; 40 mg/kg imidazole ketone erastin (IKE) (#27088, Cayman Chemical, Ann Arbor, MI, USA) was injected intraperitoneally every 2 days to induce ferroptosis; 300 mg/kg 2-deoxy-d-glucose (2-DG) (S4701, Selleck Chem) was injected intraperitoneally every 2 days to inhibit glycolysis; 1 g/kg sodium L-lactate (Nala) (L7022, Sigma-Aldrich) was injected intraperitoneally every 2 days for exogenous lactate supplementation; 100 mg/kg mevalonic acid lithium salt (MVA-Li) (#50838, Sigma-Aldrich) was injected intraperitoneally every day for exogenous MVA supplementation.

Following the therapeutic intervention, tumor weight, body weight, and tumor volume (calculated as tumor volume =  $0.5 \times \text{tumor length} \times \text{tumor width}^2$ ) was determined. Quantification of intratumoral malondialdehyde (MDA) levels was performed using the Lipid Peroxidation (MDA) Colorimetric/Fluorometric Assay Kit (K739, Biovision, Milpitas, CA, USA) according to the manufacturer's protocol. IHC was also conducted to examine CD8<sup>+</sup> T cell infiltration within tumor tissues (anti-mouse CD8a, 1:500 for IHC, # 98941T, Cell Signaling Technology, Danvers, MA, USA).

## 2.9 | Flow cytometry analysis

Fresh tumor tissues were processed into single cell suspensions using a 70  $\mu\text{m}$  cell strainer. Mouse tumor-infiltrating lymphocytes (TILs) were isolated using density gradient centrifugation with 40%/80% Percoll medium (17089101, GE Healthcare, Chicago, IL, USA). For cytokine analysis, TILs were incubated with phorbol 12-myristate 13-acetate (PMA) (10 ng/mL, S7791, Selleck Chem), Ionomycin (1  $\mu\text{g}/\text{mL}$ , S7074, Selleck Chem), Brefeldin A (1:1,000, S7046, Selleck Chem), and Monensin (1:1,000, S2324, Selleck Chem) at 37°C for 5 h. Dead cells were identified using Fixable Viability Stain 700 (1:200, 564997, BD Biosciences, San Jose, CA, USA). Surface staining was performed with antibodies against CD45 (1:200, 557659, BD Biosciences), CD3 (1:200, 564379, BD Biosciences), CD4 (1:200, 563747, BD Biosciences), and CD8 (1:200, 563068, BD Biosciences). Cells were then fixed and permeabilized using Transcription Factor Buffer Set (562574, BD Biosciences) at room temperature for 30 min, followed by intracellular staining for IFN $\gamma$  (1:200, 557649, BD Biosciences) and TNF $\alpha$  (1:200, 554419, BD Biosciences). Post-staining, cells were fixed in 4% formaldehyde. Flow cytometric analysis was conducted using CytoFLEX flow cytometer (Beckman, Brea, CA, USA), and data were analyzed using FlowJo 10.0 software (FlowJo, LLC, Eugene, OR, USA).

## 2.10 | Co-culture of T cells and ICC tumor cells for ferroptosis assessment

OT-1 T cells were isolated from OT-1 transgenic mice (#003831, The Jackson Laboratory, Bar Harbor, ME, USA) using the CD8a<sup>+</sup> T Cell Isolation Kit (130-096-543, Miltenyi, Bergisch Gladbach, Germany) as per the manufacturer's protocol. The cells were cultured in RPMI 1640 medium supplemented with 2 mmol/L glutamine (#25030081, Gibco), 10% FBS, 1 $\times$  penicillin/streptomycin, 1 mmol/L pyruvate (#11360070, Gibco), 50 mmol/L 2-mercaptoethanol (M3148, Sigma-Aldrich), 1 $\times$  MEM Amino Acids Solution (#11130051, Gibco), and 20 ng/mL mouse interleukin-2 (IL-2) (212-12-20UG, Peprotech). Activation of OT-1 T cells was carried out with Dynabeads Mouse T-Activator CD3/CD28 (11452D, Invitrogen) for 6 days.

For human epidermal growth factor receptor 2 (HER2)-specific chimeric antigen receptor T-cells (anti-hHER2-CAR-T cells), the CAR constructs targeting hHER2 and CD19 were designed as reported [27]. Briefly, the CAR construct was designed with the single-chain variable fragment of HER2 (from the 4D5 monoclonal antibody) fused to the CD8 $\alpha$ -chain hinge, transmembrane region, and intracellular signaling domains of CD3 $\zeta$  and CD28, integrated into a lentiviral vector from Obio Bioscience (Shanghai, China). CD8<sup>+</sup> T cells were activated with Dynabeads Human T-Activator CD3/CD28 (11161D, Invitrogen) and supplemented with 100 U/mL recombinant human IL-2 (200-02-50UG, Peprotech) in TexMACS Good Manufacturing Practice medium (170-076-306, Miltenyi). On day 2 post-activation, lentiviral transduction was performed at a multiplicity of infection of 1:10 using lentivirus-containing supernatants on RetroNectin (T100, Takara Bio, Kusatsu, Shiga, Japan)-coated plates. After centrifugation (1,000  $\times g$  for 2 h at 32°C), cells were incubated at 37°C for 6 h. Transduction efficiency was measured by flow cytometry on days 3 and 5 after lentivirus transduction.

For co-culture, pLV3-CMV-mOVA-EF1a-Puro plasmid (P69517, Miaoling Plasmid, Wuhan, Hubei, China) had been transiently transfected into KP-ICC cells using Neofect Transfection Reagent (TF201201, Genomtech, Beijing, China) following the manufacturer's protocol. After 72 h of transfection, cells were selected with 5  $\mu\text{g}/\text{mL}$  puromycin (P8230, Solarbio) for 3 days to obtain ovalbumin (OVA)-overexpressed KP-ICC cells. And then, OVA-overexpressed KP-ICC cells or HER2<sup>+</sup> human ICC HuCCT-1 cells were plated in 12-well plates (50,000 or 100,000 cells/well) with 100 ng/mL IFN $\gamma$  (Mouse Recombinant IFN $\gamma$  Protein, # 315-05, Peprotech; Human Recombinant IFN $\gamma$  Protein, #300-02, Peprotech). Activated OT-1 T cells or anti-hHER2-CAR-T cells were added the following day at

1:1 effector-to-target ratios. After 48 h of co-culture, T cells were removed, and cancer cells were counted.

Ferroptosis and cell viability were assessed by dissociating the co-cultured cancer cells, rinsing them with phosphate-buffered saline (PBS), and staining with BODIPY 581/591 C11 (D3861, Invitrogen) for 30 min at 37°C, protected from light. Cells were then resuspended in PBS with 7-aminoactinomycin D (7-AAD) (559925, BD Biosciences) and analyzed using a CytoFLEX flow cytometer.

## 2.11 | Plasmid construction

The pLKO.1-scramble and pLKO.1-mPck1 shRNA plasmids were constructed by annealing and cloning 2 target double-stranded oligonucleotides (shRNA #1/ #2 sequences) and 1 non-targeting sequence (negative control, scramble) into the pLKO.1 vector (#8453, Addgene). The shRNA sequences were as follows: mPck1 shRNA #1, 5'-ATCCGCAAGCTGAAGAAATAT-3'; mPck1 shRNA #2, 5'-ACAAATCCAAAT GCCATTAAA-3'.

To generate hPCK1 knock-out ICC cell lines, sgRNAs targeting hPCK1 were cloned into PX330 (#42230, Addgene) or LentiCRISPR v2 (#52961, Addgene). The sgRNA sequences were hPCK1-sgRNA #1, 5'-gTGCCTTTCAGATCTGCTCA-3', and hPCK1-sgRNA #2, 5'-gGGATAAGAACCACAGAACAC-3'.

For functional studies of post-translational modifications, human and mouse PCK1 (WT/S90A/S90D/C288S), lactate dehydrogenase A (LDHA) (WT/T248A), and sterol regulatory element-binding protein (SREBP) regulating gene protein (SPRING) (WT/K82R) were PCR-amplified and cloned into pcDNA3.1/hygro(+)-Flag, -HA, -Myc (gifts from the Hepatic Surgery Center, Tongji Hospital, Huazhong University of Science and Technology), pT3-EF1 $\alpha$  (#180149, Addgene), and pET32a vectors (P0033, Miaoling Plasmid).

For proximity labeling, SPRING was cloned into the Flag-TurboID vector (124646, Addgene), which was provided by Fengqian Li (Stony Brook University, New York, NY, USA).

## 2.12 | Plasmid and siRNA transfection

For transient transfection, cells were plated at a density of  $4 \times 10^5$  per 60-mm dish or  $1 \times 10^5$  per well of a 6-well plate approximately 18 h before transfection. Plasmid transfections were performed using Neofect Transfection Reagent according to the manufacturer's protocol. siRNA transfections were performed using Lipomaster 3000 Transfection Reagent (TL301, Vazyme) according to the manufacturer's protocol. Penicillin and streptomycin

were removed from the culture medium during the transfection process. For stable transfection, viral production, infection, and the establishment of stable cell clones have been previously described [28]. The siRNA sequences used for siRNA transfections are listed below: si-coenzyme Q2 (CoQ<sub>2</sub>), 5'-CCATAGGAACCT GGCTGCTGTATTT-3'; si-UbiA prenyltransferase domain containing 1 (UBIAD1), 5'-GGGCCGGCAATTTGGTCAACACATA-3'.

## 2.13 | Generation of PCK1 knockout cell lines

*PCK1-KO* HuCCT-1 cells were generated via transient transfection of PX330-(sg hPCK1 #1/ #2) into HuCCT-1 cells at 60% confluence using Neofect Transfection Reagent. For *PCK1-KO* QBC939/RBE/SK-ChA-1 cells generation, cells were infected with LentiCRISPR v2-based lentivirus containing sg hPCK1 #1/ #2 in the presence of polybrene (0.8  $\mu$ g/mL, HY-112735, MedChemExpress). After 48h, all transfected or infected cells were selected with puromycin (HuCCT-1, 2  $\mu$ g/mL; QBC939, RBE, SK-ChA-1, 5  $\mu$ g/mL) for 3 days.

Transfected cells were subsequently trypsinized, diluted for single-cell cloning, and seeded into 96-well plates. Genomic DNA was extracted from each clone, and PCR products spanning the knockout sites (200-300 bp) were subjected to NGS for genotyping. The primers used for NGS were 5'-CAGGGTGCTGGGACAGGCAG-3' (forward) and 5'-GGCCTGAACCTCTCGGCCAA-3' (reverse). Following the establishment of *PCK1-KO* HuCCT-1 cells, recombinant PCK1<sup>WT</sup>, PCK1<sup>S90A</sup>, or PCK1<sup>S90D</sup> was re-overexpressed using lentivirus (DesignGene-Bio, Shanghai, China).

## 2.14 | Generation of PCK1, LDHA, and SPRING mutation cell lines

To mimic phosphorylation deficiency/activation of PCK1 S90, phosphorylation deficiency of LDHA T248, and lactylation deficiency of SPRING, mouse and human PCK1 S90A/S90D mutation, LDHA T248A mutation, and SPRING K82R mutation cell lines were generated as previously described [29]. Briefly, for prime editing, enhanced prime-editing guide RNAs (epgRNAs) and nicking sgRNAs were designed using PrimeDesign [30]. The epgRNAs were cloned into the pU6-tevopreq1-GG-acceptor vector (174038, Addgene), and the nicking sgRNAs were cloned into the pU6-pegRNA-GG-acceptor vector (132777, Addgene).

HuCCT-1 and KP-ICC cells were seeded at a density of  $1 \times 10^5$  cells per well in 6-well plates approximately 18 h prior

to transfection. Subsequently, 1.6  $\mu\text{g}$  Prime Editing Max-Blastcidin (#174821, Addgene), 0.198  $\mu\text{g}$  epegRNA, 0.088  $\mu\text{g}$  nick RNA, and 0.8  $\mu\text{g}$  pEF1a-hMLH1dn (#174824, Addgene) were co-transfected into cells using Neofect Transfection Reagent, following the manufacturer's protocol. After 72 h of transfection, cells were selected with 5  $\mu\text{g}/\text{mL}$  blasticidin (ant-bl-05, InvivoGen) for 3 days.

The surviving cells were trypsinized, and cells were diluted to 1 cell per well in 96-well plates to ensure single-cell cloning. Genomic DNA was extracted from successfully expanded clones, and PCR amplification was performed to validate the edits. The amplified PCR products spanned at least 25 bp upstream of the epegRNA-guided nick RNA site to 25 bp downstream of the 3' flap generated by the RT or any secondary nick RNA. Primers used for genotyping are listed in Supplementary Table S3.

## 2.15 | Lipid peroxidation and cell viability analysis

For lipid peroxidation analysis, cells ( $1.5 \times 10^5$  per well) were plated in 12-well plates and treated with the following compounds: cisplatin (1  $\mu\text{mol}/\text{L}$ , 36 h), gemcitabine (5  $\text{nmol}/\text{L}$ , 36 h); cell death inhibitors Lip1 (300  $\text{nmol}/\text{L}$ , 36 h), deferoxamine (DFO) (ferroptosis inhibitor, S5742, Selleck-Chem, 5  $\mu\text{mol}/\text{L}$ , 36 h), Z-Val-Ala-Asp(OMe)-fluoromethylketone (Z-VAD-FMK) (apoptosis inhibitor, S7023, Selleck-Chem, 10  $\mu\text{mol}/\text{L}$ , 36 h), and necrostatin-1s (Nec-1) (necroptosis inhibitor, S8641, Selleck-Chem, 2  $\mu\text{mol}/\text{L}$ , 36 h), which were all administered 1 h before RSL3 treatment; Glutathione peroxidase 4 (GPX4)-glutathione (GSH) system inhibitors RSL3 (10  $\mu\text{mol}/\text{L}$ , 36 h), erastin (S7242, Selleck-Chem, 10  $\mu\text{mol}/\text{L}$ , 36 h), FINO2 (25096, Cayman Chemical, 10  $\mu\text{mol}/\text{L}$ , 36 h), ML210 (23282, Cayman Chemical, 1  $\mu\text{mol}/\text{L}$ , 36 h), and ML162 (20455, Cayman Chemical, 10  $\mu\text{mol}/\text{L}$ , 36 h); ferroptosis suppressor protein 1 (FSP1)-CoQ<sub>10</sub>H<sub>2</sub> system inhibitors ferroptosis-inducing agent 56 (FIN56) (25180, Cayman Chemical, 10  $\mu\text{mol}/\text{L}$ , 36 h), and simvastatin (10  $\text{nmol}/\text{L}$ , 36 h), iFSP1 (S9663, Selleck-Chem, 200  $\text{nmol}/\text{L}$ , 36 h); and other compounds GSK 2837808A (LDHA-specific inhibitor, S8590, Selleck-Chem, 10  $\text{nmol}/\text{L}$ , 36 h), 2-DG (glycolysis inhibitor, 10  $\text{mmol}/\text{L}$ , 36 h), MVA-Li (500  $\mu\text{mol}/\text{L}$ , 36 h), Nala (10  $\text{mmol}/\text{L}$ , 36 h) and PPB peptide (1  $\mu\text{g}/\text{mL}$ , 36 h), sodium pyruvate (HY-W015913, MedChemExpress, 10  $\text{mmol}/\text{L}$ , 36 h), glucose (G7021, Sigma-Aldrich, 10  $\text{mmol}/\text{L}$ , 36 h). Post the indicated treatments, the cells were collected, stained with 5  $\mu\text{mol}/\text{L}$  BODIPY 581/591 C11 at 37°C for 30 min, and analyzed by flow cytometry. The signals from both non-oxidized [phycoerythrin (PE) channel] and oxidized [fluorescein isothiocyanate (FITC) channel] C11 were monitored. The fluorescence intensity ratio (FITC:PE) was

calculated for each sample. At least 5,000 cells were analyzed in each group, and all experiments were repeated thrice.

For cell viability analysis, cells ( $3 \times 10^3$  per well) were plated in 96-well plates. After the indicated treatments, cell viability was assessed using Cell Counting Kit-8 (CCK-8) (A311, Vazyme) for 2D-cultured cells or CellTiter-Glo (G9681, Promega, Madison, Wisconsin, USA) for BME-coated organoid cells, following the manufacturer's protocol. The compounds used for cell viability analysis were a subset of those assessed in the lipid peroxidation assay. The percentage of cell viability measured by CCK-8 assay was calculated as follows: cell viability (%) =  $[(A_{450\_sample} - A_{450\_blank}) / (A_{450\_control} - A_{450\_blank})] \times 100\%$  [sample: cells with indicated compounds; control: DMSO-treated cells; blank: medium-only (no cells/drugs)]; the percentage of cell viability measured by CellTiter-Glo assay was calculated as follows: cell viability (%) =  $[(RLU\_sample - RLU\_blank) / (RLU\_control - RLU\_blank)] \times 100\%$  [Luminescence signals (relative light units, RLU)].

## 2.16 | Cell death evaluation

We used 7-AAD/propidium iodide (PI) (A211, Vazyme) or SYTOX Red Dead Cell Stain (S34859, Invitrogen), followed by flow cytometry analysis or fluorescence microscope (Eclipse-Ti2, Nikon, Tokyo, Japan) to detect cell death. Cells were seeded in 12-well plates at a density of  $1.5 \times 10^5$  cells per well. On Day 2, the cells were treated with the indicated compounds. The compounds used for cell death evaluation were a subset of those assessed in the lipid peroxidation assay. For 7-AAD/PI staining, the viable and floating dead cells were collected, stained with 5  $\mu\text{g}/\text{mL}$  7-AAD/PI for 5 min, and analyzed by flow cytometry. For SYTOX staining, the medium was replaced with fresh medium containing 30  $\text{nmol}/\text{L}$  SYTOX Red Dead Cell Stain and incubated at 37°C for 15 min. Then, the plates were immediately transferred to the fluorescence microscope, and 5 images per well were captured in the red and phase channels. The ratio of SYTOX Red-positive objects (dead cells) to phase objects (total cells) was quantified using ImageJ software (National Institutes of Health, Bethesda, MD, USA).

## 2.17 | Immunoprecipitation liquid chromatography-tandem mass spectrometry (IP-LC-MS/MS) analyses

The bead samples of IP were resuspended in PBS and submitted to Spec-Ally Biotechnology (Wuhan, Hubei, China)

for the following MS analysis. Briefly, bead samples were incubated in the reaction buffer [1% sodium deoxycholate (SDC), 100 mmol/L Tris-HCl (pH 8.5), 10 mmol/L tris(2-carboxyethyl)phosphine (TCEP), 40 mmol/L chloroacetamide (CAA)] at 95°C for 10 min for protein denaturation, cysteine reduction, and alkylation. The eluate was diluted with an equal volume of H<sub>2</sub>O and subjected to trypsin digestion overnight by adding 1 µg of trypsin at 37°C. The peptide was purified using self-made SDB desalting columns. The eluate was vacuum-dried and stored at -20°C for later use.

LC-MS/MS data acquisition was performed on a Q Exactive HF-X mass spectrometer coupled with an Easy-nLC 1200 system (Thermo Scientific) as described previously [31]. Briefly, peptides were first loaded onto a C18 trap column and then eluted into a C18 analytical column (75 µm × 25 cm, 2 µm particle size, 100 Å pore size, Acclaim PepMap C18 column, Thermo Scientific). Mobile phase A (0.1% formic acid) and mobile phase B [80% acetonitrile (ACN), 0.1% formic acid] were used to establish the analysis gradient. A constant flow rate was set at 300 nL/min. For data-dependent acquisition mode analysis, each scan cycle consisted of 1 full-scan mass spectrum [resolution (R) = 60 K, automatic gain control (AGC) = 3e<sup>6</sup>, max ion injection time (IT) = 20 ms, scan range = 350-1800 m/z] followed by 20 MS/MS events (R = 15 K, AGC = 2e<sup>5</sup>, max IT = 50 ms). The higher energy collision-induced dissociation collision energy was set to 25. The isolation window for precursor selection was set to 1.6 Da. The former target ion exclusion was set for 35 s. MS raw data were analyzed with MaxQuant (V1.6.6) [32] using the Andromeda database search algorithm [33]. Spectra files were searched against the UniProt Human proteome database [34] using the following parameters: Variable modifications, Oxidation (M) & Acetyl (Protein N-term); Fixed modifications, Carbamidomethyl (C); Digestion, Trypsin/P. Search results were filtered with 1% false discovery rate at both protein and peptide levels.

## 2.18 | IC50 determination assay

Cells were seeded into 96-well plates at a density of 20,000 cells per well and cultured overnight to allow attachment. Serial dilutions of gemcitabine (0-60 nmol/L, 8 concentrations), cisplatin (0-20 µmol/L, 8 concentrations), and RSL3 (0-100 µmol/L, 8 concentrations) were prepared in culture medium with a 2-fold interval between adjacent concentrations and added to the wells. Cells were incubated for 48 h at 37°C under 5% CO<sub>2</sub>.

Cell viability was assessed using the CCK-8 assay. Dose-response curves were generated, and IC50 values (the concentration of the compound that inhibits 50% of cell

growth) were determined using nonlinear regression analysis with GraphPad Prism8 software (GraphPad Software, Inc., Boston, MA, USA). Experiments were performed in triplicate and repeated at least three times independently.

## 2.19 | Phosphoenolpyruvate carboxykinase (PEPCK) activity measurements

Canonical PEPCK activity, converting oxaloacetate to phosphoenolpyruvate using guanosine triphosphate (GTP), was measured using the Phosphoenolpyruvate Carboxykinase Activity Assay Kit (Colorimetric) (K359, Biovision), following the manufacturer's instructions.

## 2.20 | Glucose uptake assay

Glucose uptake was measured using 2-(N-(7-nitrobenz-2-oxa-1,3-diazol-4-yl) amino)-2-deoxyglucose (2-NBDG) (N13195, Invitrogen). HuCCT-1, HCCC-9810, QBC939, and RBE cells were incubated with 100 µmol/L 2-NBDG for 2 h, followed by fluorescence intensity analysis via flow cytometry.

## 2.21 | Intracellular lactate detection

Intracellular lactate levels were measured using the Lactate Colorimetric/Fluorometric Assay Kit (K607, Biovision), following the manufacturer's protocol.

## 2.22 | Assessment of extracellular acidification rate (ECAR)

The ECAR was measured using Seahorse XFp Glycolytic Rate Assay Kit (103346, Agilent, Santa Clara, California, USA) on Seahorse XF24 analyzer (Agilent). Cells (1 × 10<sup>5</sup> per well) were seeded into Seahorse XF24-well culture plates in RPMI 1640 and incubated overnight at 37°C with 5% CO<sub>2</sub>. Cells were washed twice with Assay Medium and incubated in the same medium at 37°C in a non-CO<sub>2</sub> incubator for 1 h before the assay.

The assay was conducted using a template created on the XF Controller, with cycles consisting of 3 min of mixing, 2 min of waiting, and 3 min of measurement. Baseline ECAR was measured twice before sequential injections of rotenone/antimycin A (0.5 µmol/L) and 2-DG (50 mmol/L) at the specified time points. Oxygen consumption and ECAR were monitored until stabilization, after which the experiment was terminated. Protein concentrations in

each well were determined using BCA Protein Assay Kit (1863381, Thermo Scientific) for normalization.

## 2.23 | Sterol regulatory element (SRE) luciferase assay

SRE luciferase activity was quantified using a dual-luciferase assay system (J308, Promega, Madison, Wisconsin, USA). Briefly, 10,000 cells per well HuCCT-1 or KP-ICC cells were seeded into 24-well plates and co-transfected the following day with 200 ng of pGL4.17-SRE and 4 ng of pRL-TK plasmids using Neofect Transfection Regents, according to the manufacturer's protocol. At 48 h after transfection, cells were treated with or without 10 mmol/L Nala or 10 mmol/L 2-DG for 24 h. Following treatment, cell lysates were analyzed for firefly and renilla luciferase activities as per the manufacturer's protocol.

## 2.24 | RT-qPCR

Total cell RNA was extracted using Trizol. According to the manufacturer's protocol, reverse transcription was carried out using HiScript II Q Select RT SuperMix (R233, Vazyme). RT-qPCR was performed using the ChamQ Universal SYBR qPCR Master Mix (Q711, Vazyme). Gene expression levels were normalized to those of actin beta (ACTB) in the same samples. Each sample was analyzed independently in triplicate. The primers used are listed in Supplementary Table S4.

## 2.25 | Lipidomics analyses

Lipids were extracted from approximately  $1 \times 10^6$  cells using a modified Bligh-Dyer method [35]. Briefly, cells were homogenized in 750  $\mu$ L of chloroform:methanol:MilliQ H<sub>2</sub>O (3:6:1, v/v/v) and incubated at 300  $\times$ g for 1 h at 4°C. Phase separation was induced by adding 350  $\mu$ L of deionized water and 250  $\mu$ L of chloroform, followed by centrifugation at 1,500  $\times$ g for 5 min at 4°C to isolate the lower organic phase containing lipids. Lipid extraction was repeated by adding 450  $\mu$ L of chloroform to the aqueous phase, and lipid extracts were pooled, dried in a SpeedVac (OH mode), and stored at -80°C. The upper aqueous phase and cell pellet were dried in a SpeedVac (H<sub>2</sub>O mode), and protein content in the pellet was quantified using the Pierce BCA Protein Assay Kit (23227, Thermo Scientific) according to the manufacturer's instructions.

Lipidomic analyses were performed at LipidALL software (LipidALL Technologies, Changzhou, Jiangsu,

China) using a Nexera 20AD-HPLC coupled with a Sciex QTRAP 6500 PLUS (Shimadzu, Kyoto, Japan), as previously described [36].

Individual lipid classes of polar lipids were separated by normal-phase high performance liquid chromatography (HPLC) on a TUP-HB silica column (150  $\times$  2.1 mm, 3  $\mu$ m) (C08, Tuplabs, Tianjin, China) under the following conditions: mobile phase A (chloroform:methanol:ammonium hydroxide, 89.5:10:0.5) and mobile phase B (chloroform:methanol:ammonium hydroxide:water, 55:39:0.5:5.5). Multiple reaction monitoring (MRM) transitions were optimized for comparative analysis of various polar lipids, and individual lipid species were quantified using spiked internal standards. Free fatty acids were quantified using d31-16:0 (860393P, Sigma-Aldrich) and d8-20:4 (390010, Cayman Chemicals).

## 2.26 | CoQ<sub>10</sub>H<sub>2</sub>/CoQ<sub>10</sub> measurements by LC-MS

The method for CoQ<sub>10</sub>H<sub>2</sub>/CoQ<sub>10</sub> measurements was adapted from a previously reported method [37]. Briefly, a cold tert-butylhydroquinone (TBHQ) solution (S4990, Selleck) was employed to inhibit auto-oxidation during sample extraction. A 1  $\mu$ mol/L TBHQ solution in propanol (100  $\mu$ L) and cold propanol (600  $\mu$ L) were added to each cell-containing tube at frozen state. Post-addition, the samples underwent a 2-min sonication and were mixed with a vortex after adding 100  $\mu$ L of CoQ<sub>9</sub> internal standard (250  $\mu$ g/L) (303-97-9, Yuanye Bio, Shanghai, China). The mixture was centrifuged at 1,500  $\times$ g and 1°C for 10 min, and the propanol supernatant was subsequently transferred to an autosampler vial for immediate LC-MS analysis.

Chromatographic separation was achieved using a LC-20AD HPLC system (Shimadzu) with a binary pump, an Ultimate XB-C18 column (50 $\times$ 2.1 mm, 5  $\mu$ m) maintained at 40°C, and methanol as the mobile phase at a flow rate of 0.8 mL/min. Each run lasted 9 min. Detection was conducted on a QTRAP 5500 mass spectrometer (AB Sciex, Framingham, MA, USA) using an electrospray ionization (ESI) source in the positive-ion mode. Optimized conditions included nitrogen gas settings at 40 psi (nebulizer), 40 psi (turbo spray), 20 psi (curtain), with a turbo gas temperature of 500°C and ESI needle voltage set to 5500 V. Analyst 1.6.2 software (AB Sciex) managed the instrument's control and data analysis.

MRM transitions were as follows:

Oxidized Coenzyme Q10:  $m/z$  863.7  $\rightarrow$  197.1, collision energy (CE) = 41 V, dwell time = 100 ms, retention time ( $t_R$ ) = 7.72 min.

Reduced Coenzyme Q10:  $m/z$  882.7  $\rightarrow$  197.1, CE = 25 V, dwell time = 100 ms, retention time ( $t_R$ ) = 4.28 min.

Oxidized Coenzyme Q9 (Internal Standard, IS):  $m/z$  795.6  $\rightarrow$  197.1, CE = 33 V, dwell time = 100 ms, retention time ( $t_R$ ) = 4.64 min.

## 2.27 | Mevalonate and MK4 measurements by LC-MS

Cell cultures for MVA and menaquinone-4 (MK4) analysis were maintained in RPMI 1640 medium for 24 h. Cells were subsequently washed with ice-cold PBS and quenched with 600  $\mu$ L of LC-MS grade methanol. Samples were stored at  $-80^\circ\text{C}$  until analysis. Metabolomic profiling was conducted using a QTRAP 5500 mass spectrometer equipped with an ESI source, following previously described methods [38, 39]. Chromatographic review and peak area integration were performed using MultiQuant software (v2.1), with metabolite quantification normalized to the internal standard's peak area within each sample.

## 2.28 | Immunoprecipitation (IP) and Western blotting (WB) analysis

Cells were collected and lysed on ice using IP lysis buffer [150 mmol/L NaCl, 50 mmol/L Tris-HCl, 1 mmol/L EDTA, 1% Nonidet P-40 (NP-40), 10% glycerol]. Lysates were incubated with protein G agarose for 2 h and immunoprecipitated with corresponding antibodies overnight at  $4^\circ\text{C}$ . The lysates were then incubated with protein A/G magnetic beads (HY-K0202, MedChemExpress) for 1 h, then washed 1 time using IP lysis buffer and washed 3 times with IP washing buffer (300 mmol/L NaCl, 1.0 mmol/L EDTA, 25 mmol/L Tris-HCl, pH7.4, 1.0% NP-40). The beads were eluted with  $2\times$  SDS-polyacrylamide gel electrophoresis (PAGE) loading buffer and subjected to WB analysis. The WB procedure was performed as previously described [28].

The antibodies used for WB and IP were as follows: anti-Tp53 (2  $\mu\text{g}/\text{mL}$ , ab26, Abcam), anti-AKT (1:1,000, #9272, Cell Signaling Technology), anti-AKT pS473 (1:1,000, #4060, Cell Signaling Technology), anti-ERK1/2 (1:1,000, #9102, Cell Signaling Technology), anti-ERK1/2 pT202/pY204 (1:1,000, #4370, Cell Signaling Technology), anti-PCK1 pS90 (1:500, Customized, Atagenix Biotechnology, Wuhan, Hubei, China), anti-PCK1 (1:1,000 for WB, 1:300 for IP, 16754-1-AP, Proteintech), anti-Beta tubulin (1:1,000, 10068-1-AP, Proteintech), anti-L-Lactyl Lysine Rabbit mAb (anti-pan-Klac 1:1,000, PTM-1401RM, PTM Bio, Hangzhou, Zhejiang, China), anti-LDHA (pT248) (1:500, Customized, Atagenix Biotechnology), anti-LDHA (1:2,000, 21799-1-AP, Proteintech), anti-SREBF1 (1:1,000,

14088-1-AP, Proteintech), anti-SREBP2 (1:1,000, ab30682, Abcam), anti-Phosphoserine/threonine (1:500, PP2551, PhosphoSolutions, Aurora, CO, USA), anti-Acetyllsine Rabbit pan-Ab (pAb) (1:500, PTM-132, PTM Bio), anti-Flag tag (1:1,000 for WB, 1:200 for IP, RA1003, Vazyme), anti-MYC tag (for IP, 1:500, 16286-1-AP, Proteintech), anti-endoplasmic reticulum protein 72 (ERp72) (1:2,000, 66365-1-Ig, Proteintech), anti-Golgi matrix protein 130 (GM130) (1:2,000, 66662-1-Ig, Proteintech), anti-FSP1 (1:1,500, 20886-1-AP, Proteintech), anti-Lysine acetyltransferase 7 (KAT7)/MYST histone acetyltransferase 2 (MYMT2) (1:2,000, 13751-1-AP, Proteintech), anti-phosphatase and tensin homolog (PTEN) (D4.3) (1:1,000, 9188, Cell Signaling Technology), anti-SPRING (1:500, H00079794-K, Abnova, Taipei, Taiwan), anti-SREBP cleavage-activating protein (SCAP) (1:1,000, ab190103, Abcam), anti-Flag (1:1,000, F1804, Sigma-Aldrich, St. Louis, Missouri, USA), and Horseradish peroxidase (HRP) Mouse Anti-Rabbit IgG light chain specific (LCS) (1:1,000, A25022), HRP Mouse Anti-Rabbit IgG heavy chain specific (HCS) (1:1,000, A25122), HRP Goat Anti-Mouse IgG LCS (1:1,000, A25012), HRP Goat Anti-Rabbit IgG HCS (1:1,000, A25222) was purchased from Abbkine Scientific (Changzhou, Jiangsu, China).

## 2.29 | Purification of recombinant proteins

His-PCK1<sup>WT</sup>, His-PCK1<sup>S90A</sup>, His-PCK1<sup>C228S</sup>, and His-AKT were expressed in bacteria and purified as described previously [40]. Myc-LDHA<sup>WT</sup> and Myc-LDHA<sup>T248A</sup> were expressed in HEK-293T and purified by using anti-MYC (EQKLISEEDL) Affinity Agarose (IP0097, Dia-an Bio, Wuhan, Hubei, China) following the manufacturer's protocols. PCK1<sup>WT</sup> and PCK1<sup>S90A</sup> were purified by anti-Flag-affinity gel from Flag-PCK1<sup>WT</sup>, or Flag-PCK1<sup>S90A</sup>/Flag-SPRING<sup>WT</sup>, or Flag-SPRING<sup>K82R</sup> overexpressed PCK1-KO HuCCT-1 cells/HEK-293T cells or subsequent elution by the addition of Flag peptide as described previously [41].

## 2.30 | Bioinformatic prediction of phosphorylation sites

Potential phosphorylation sites on LDHA were predicted using SCANSITE [42] and PhosphoSite [43] following the authors' recommended protocols. Overlapping predictions from both tools were analyzed to identify high-confidence candidate phosphorylation sites on LDHA. Candidate sites were further verified through alanine-scanning mutagenesis and WB with phospho-specific antibodies.

### 2.31 | LDHA enzymatic assay

Purified Myc-LDHA<sup>WT</sup> or Myc-LDHA<sup>T248A</sup> proteins (500 ng per reaction) were added to a reaction buffer containing 0.2 mol/L Tris-HCl (pH 7.3), 1 mmol/L pyruvate, and 0.2 mmol/L nicotinamide adenine dinucleotide (reduced form) (NADH). For enzyme kinetics, the buffer included 2 mmol/L pyruvate and varying NADH concentrations (0–0.6 mmol/L). NADH oxidation was monitored at 340 nm (absorbance) using Multiskan FC Microplate Spectrophotometer (Thermo Scientific).

### 2.32 | In vitro kinase assay

For the in vitro kinase assay, 1 µg His-PCK1<sup>WT/S90A/C288S</sup> bound to nickel-nitrilotriacetic acid (Ni-NTA) agarose beads (30230, Qiagen, Hilden, North Rhine-Westphalia, Germany) was incubated with or without 1 µg His-AKT and 100 µmol/L adenosine triphosphate (ATP) (#9804, Cell Signaling Technology) for 1 h. After washing with PBS, beads were incubated with Myc-LDHA<sup>WT/T248A</sup> in kinase buffer (50 µL) containing 0.5 mmol/L GTP (HY-113225, MedChemExpress) at 25°C for 1 h. Reactions were terminated with SDS-PAGE loading buffer, heated at 100°C for 5 min, and analyzed via SDS-PAGE. To confirm PCK1 phosphorylation's role in LDHA binding, 10 U calf intestinal alkaline phosphatase (CIP) (M0525, NEB, Ipswich, MA, USA) was added post-AKT kinase assay to remove the phosphorylation of PCK1.

### 2.33 | Immunofluorescence analysis

Immunofluorescence analysis was performed as previously reported [28]. In brief, cells were cultured on coverslips for 12 h after the indicated treatments, fixed in 4% paraformaldehyde for 15 min at room temperature, and permeabilized with 0.5% Triton X-100 for 5 min, then blocked in 5% BSA for 1 h. After blocking, the slides were incubated according to the primary antibody overnight at 4°C in a humidified box. Afterward, the slides were washed 3 times and incubated with a secondary antibody overnight at 4°C in a humidified box. Finally, cell nuclei were stained by 4',6-diamidino-2-phenylindole (DAPI) (G1012, Servicebio, Wuhan, Hubei, China) for 5 min. Pictures were obtained and viewed using a confocal microscope (Olympus FV1000).

The primary antibodies used for immunofluorescence analysis were anti-PCK1 (1:200), anti-LDHA (1:500), anti-SCAP (1:100), anti-GM130 (1:1,000), anti-SREBP2 (1:200), anti-insulin induced gene 2 (INSIG2) (1:200, 24766-1-

AP, Proteintech), anti-SPRING (1:100), and anti-KAT7 (1:500).

### 2.34 | Subcellular fractionation

Subcellular fractionation was performed as previously described [40]. Briefly,  $1 \times 10^6$  cells HuCCT-1 cells were cultured in 2 10-cm dishes and treated with or without 10 mmol/L Nala or 10 mmol/L 2-DG for 24 h, then cells were washed twice with ice-cold PBS and homogenization buffer containing 10 mmol/L triethanolamine, 10 mmol/L acetic acid, pH 7.4, 250 mmol/L sucrose, 1 mmol/L sodium EDTA, and 1× protease inhibitor cocktail (4693116001, Roche, Basel, Switzerland) and collected in 0.8 mL of homogenization buffer. Then the buffer was homogenized by passing the cells through a 25-gauge needle on a 1-mL syringe 12 times.

The post-nuclear supernatant, obtained by centrifugation at 1,500 ×g for 15 min at 4°C, was layered onto preformed iodixanol gradients (2.65 mL each of 24%, 19.33%, 14.66%, and 10% iodixanol, prepared by diluting a 60% stock with cell suspension medium containing 0.85% NaCl and 10 mmol/L Tricine-NaOH, pH 7.4). Gradients were equilibrated at room temperature for 2 h before ultracentrifugation at 12,000 ×g for 4 h at 4°C in an Optima XE-90 Ultracentrifuge (Beckman). The post-nuclear supernatant was then centrifuged for 1.5 h at 151,000 ×g (no brake during deceleration).

A total of 15 fractions (800 µL each) were collected from the top to the bottom, excluding the bottom 2 fractions containing aggregated material. The remaining 13 fractions were analyzed by WB.

### 2.35 | Proximity labeling with TurboID

TurboID [44] was used to identify acyltransferases that interact with SPRING in HuCCT-1 WT and PCK1<sup>S90A</sup> cells. Briefly, HuCCT-1-WT and PCK1<sup>S90A</sup> HuCCT-1- cells were cultured in 15-cm dishes for 18–24 h to approximately 90% confluency. Cells were transiently transfected with the Flag-SPRING-TurboID plasmid using Neofect transfection reagents for 24 h. Biotin labeling was initiated by adding biotin (S3130, Selleck-Chem) to a final concentration of 50 µmol/L for 6 h. Labeling was terminated by placing the cells on ice and washing 5 times with ice-cold DPBS.

Cell pellets were collected and lysed on ice for 30 min using IP lysis buffer. Lysates were clarified by centrifugation at 20,000 ×g for 10 min at 4°C. The supernatant was incubated with streptavidin magnetic beads (50 µL beads per sample) (N512, Vazyme) at 4°C for 1 h with gentle

rotation to enrich biotinylated peptides. The beads were then washed 5 times with ice-cold DPBS to remove non-specifically bound proteins. After washing, the beads were resuspended in PBS and submitted to MS analysis.

### 2.36 | In vitro lactylation assay

KAT7-HA protein and Flag-SPRING (wild type or K82R) were produced in HEK-293T cells and purified using anti-HA (KAP0063, Dia-an Bio) or anti-Flag affinity beads (KAP0064, Dia-an Bio), respectively. To reduce basal lactylation, HEK-293T cells were treated with 10 mmol/L 2-DG for 36 h before purification. Lactylation assays included 500 ng of Flag-SPRING (WT or K82R) and 500 ng of HA-KAT7 in a buffer [50 mmol/L HEPES, 30 mmol/L KCl, 0.25 mmol/L EDTA, 5 mmol/L MgCl<sub>2</sub>, 5 mmol/L sodium butyrate, 20 μmol/L Lactyl-CoA (HY-141540, Med-ChemExpress), pH 7.8] at 30°C for 30 min. Reaction products were analyzed via 10% SDS-PAGE followed by WB.

### 2.37 | IHC analysis and histological evaluation of mouse and human ICC specimens

To confirm the ICC identity of the KP-ICC cell line, IHC was performed to detect the expression of HNF4A (1:2,000, ab181604, Abcam), CK19 (1:500, ab52625, Abcam), and SOX9 (1:1,000, AB5535, Sigma-Aldrich), utilizing specific antibodies as per the manufacturer's protocols.

For the IHC analyses in ICC patients, we utilized 2 distinct cohorts. The TJH-ICC-CIT cohort was comprised of tissue samples from 36 patients diagnosed with ICC who had undergone at least 2 cycles of CIT, consisting of gemcitabine, cisplatin, and durvalumab, prior to surgical tumor resection at Tongji Hospital, Huazhong University of Science and Technology between December 2019 and May 2023. The samples were employed to assess the prognostic significance of pAKT-pPCK1 levels in the context of CIT. The TJH-ICC-TMA cohort was established using 2 tissue microarrays (TMA-A: 68 cases; TMA-B: 73 cases), comprising 141 tumor samples from 112 ICC patients who underwent surgical resection at Tongji Hospital, Huazhong University of Science and Technology between January 2013 and May 2019. Due to the limited availability of this rare cohort, marker-specific staining strategies were implemented: pPCK1 was assessed across all 141 cases (TMA-A + TMA-B), whereas pAKT and pan-Klac were analyzed only in TMA-A (68 cases). As such, correlative expression patterns of pAKT, pPCK1, and pan-Klac were primarily analyzed within the TMA-A subset.

Among the total cohort, follow-up data were available for 121 cases (58 from TMA-A; 63 from TMA-B). Consequently, survival analyses were stratified by marker availability: (1) pPCK1 prognostic analysis included all 121 cases with follow-up; (2) pAKT prognostic analysis was restricted to the 58 cases from TMA-A with matched follow-up. The histopathological examination was conducted by 3 pathologists who were blinded to the patients' clinical data, with a diagnostic consensus reached through collaborative discussions. This cohort was designed to investigate the correlative expression patterns of pAKT, pPCK1, and pan-Klac and to evaluate the prognostic relevance of the pAKT-pPCK1 axis in ICC progression. Paraffin-embedded human ICC sections were stained with antibodies against PCK1 (pS90, 1:300), AKT (pS473, 1:200), pan-Klac (1:500), or non-specific IgG (#5415, 1:500, Cell Signaling Technology) as a negative control. Tissue staining was quantitatively scored based on the percentage of positive cells and staining intensity as previously described [40]. Briefly, the following proportion scores were applied: 0 for 0%, 1 for 0.1%-1.0%, 2 for 1.1%-10.0%, 3 for 10.1%-30.0%, 4 for 30.1%-70.0%, and 5 for 70.1%-100% of positive tumor cells. Staining intensity was rated on a scale of 0-3: 0 (negative), 1 (weak), 2 (moderate), and 3 (strong). Proportion and intensity scores were added to yield a total score (range: 0-8). The histological examination was performed independently by 3 experienced pathologists who were blinded to the clinical data of the patients to ensure unbiased evaluation. Any discrepancies between the pathologists were resolved through discussion to reach a consensus diagnosis.

Protein expression was classified as high or low based on a cutoff total score of 4 (low, 0-3; high, 4-8). This cutoff was determined based on the median total score across all patient samples, consistent with prior studies evaluating similar immunohistochemical markers [45]. Scores were compared to overall survival duration, defined as the time from the date of diagnosis or treatment initiation to death or the last known follow-up.

### 2.38 | PROGENy and Compass analysis

To elucidate the relationship between PI3K-AKT activation and the MVA pathway in ICC cells, we integrated single-cell RNA sequencing (scRNA-seq) data from 3 datasets: scPLC (PRJCA007744), GSE125449, and GSE142784 [46-48]. We then employed Hierarchical Cell Annotation (HCA) package to extract tumor cells, followed by batch effect correction and normalization [49], finally a dataset comprising 41,419 ICC cells from 47 ICC patients were used for subsequent analyses. To assess PI3K-AKT pathway activity, we utilized PROGENy, a tool designed to infer pathway activity from gene expression data [50].

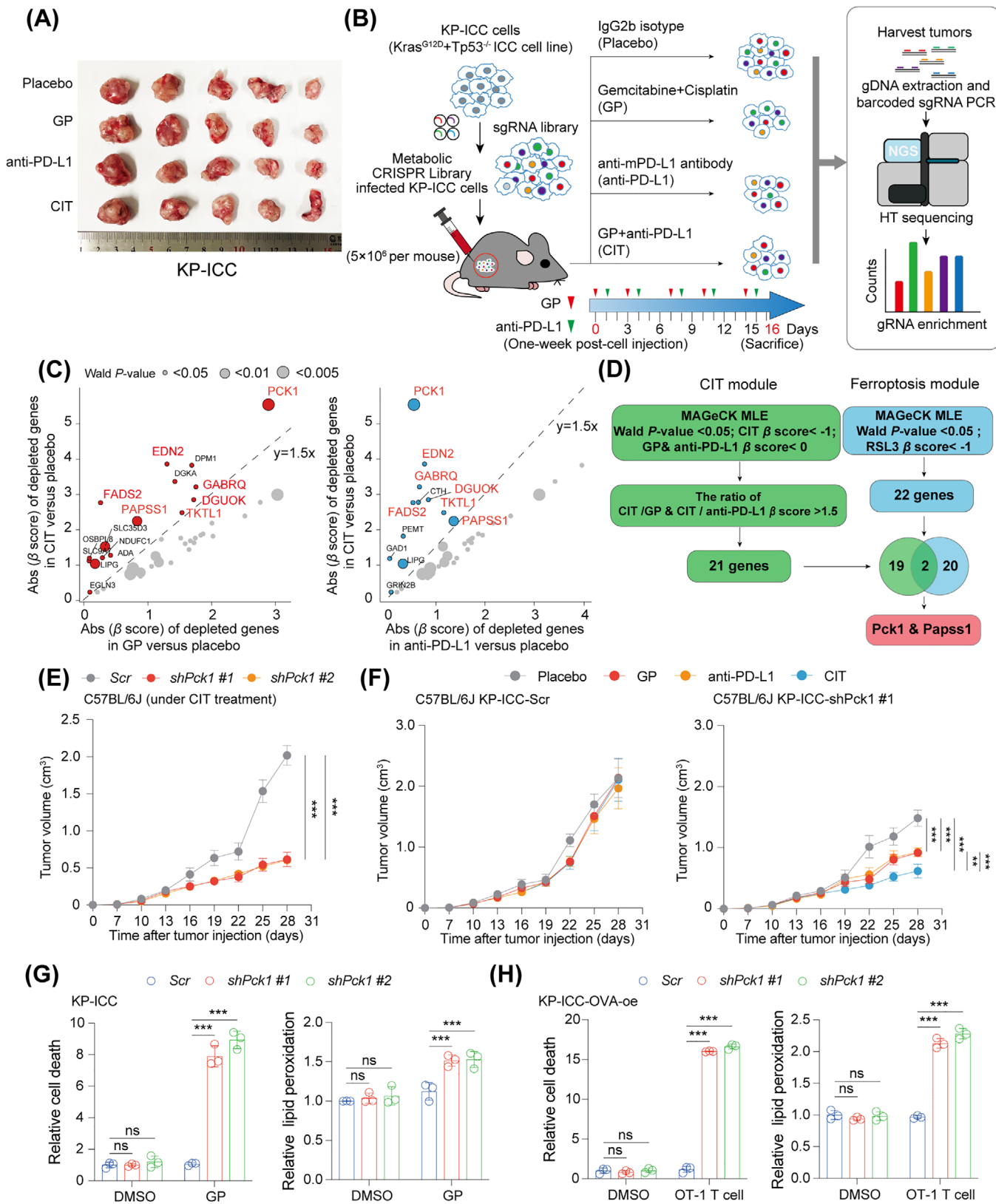


**FIGURE 1** In vivo metabolic screening reveals ferroptosis regulators of CIT in ICC. (A) Representative tumor images of C57BL/6J mice bearing subcutaneous KP-ICC tumors after indicated treatments (Placebo, GP, anti-PD-L1, or CIT;  $n = 5$  per group). (B) In vivo CRISPR screening workflow. Male C57BL/6J mice (4-5 weeks) were injected with KP-ICC cells transfected with a mouse metabolic CRISPR library. Tumors were analyzed by NGS-based sgRNA sequencing to identify regulators. Treatment groups are detailed in (A). (C) Scatter plots of absolute  $\beta$  scores (Wald  $P < 0.05$ ) for CIT-depleted genes versus GP (left) or anti-PD-L1 (right). Red/blue points: CIT/GP or CIT/anti-PD-L1

Metabolic pathway activities within tumor cells were evaluated using Compass, an algorithm that characterizes cellular metabolic states based on single-cell RNA-seq and flux balance analysis [51]. We then compared the metabolic activities between the top and bottom thirds of ICC cells, stratified by PI3K-AKT activity levels.

## 2.39 | Statistical analysis

Statistical analyses were conducted utilizing GraphPad Prism8 software. Data are represented as individual data points, mean values  $\pm$  standard deviation, as appropriate. For comparisons between 2 independent groups, unpaired 2-tailed t-tests were performed, under the assumption of normal distribution and variance homogeneity. When comparing multiple experimental groups, two-way analysis of variance (ANOVA) was employed, followed by Tukey's and Šidák's multiple comparison post-hoc tests to adjust for the risk of type I errors. Survival rates were analyzed using the Kaplan-Meier estimator, with the log-rank test applied to assess the statistical significance of differences between survival curves. A *P* value of  $<0.05$  was considered statistically significant.

## 3 | RESULTS

### 3.1 | Metabolic CRISPR screens revealed PCK1 as a crucial ferroptosis regulator modulating CIT resistance in ICC

To identify the metabolic regulators that affect tumor responses to CIT in ICC, we developed and characterized 2 murine ICC cell lines, KP-ICC and KP2. These cell lines were derived from a *Kras*<sup>G12D</sup>/*Tp53*<sup>-/-</sup> genetically engineered mouse model of ICC. KP-ICC exhibited stable tumorigenic potential in mice (Supplementary Figure S1A).

KP-ICC shared significant genetic and transcriptomic similarities with the recently reported KPPC cell line [16] that was also derived from the *Kras*<sup>G12D</sup>/*Tp53*<sup>-/-</sup> ICC mouse model (Supplementary Figure S1B-C). Additionally, KP-ICC exhibited characteristic features of *Kras*<sup>G12D</sup>/*Tp53*<sup>-/-</sup> ICC tumors, including *Tp53* loss and the downstream activation of *Kras* pathways (AKT and extracellular signal-regulated kinase 1/2 [ERK1/2]) (Supplementary Figure S1D). IHC analysis demonstrated that KP-ICC-derived subcutaneous tumors exhibited CK19<sup>+</sup>, SOX9<sup>+</sup>, and HNF4A<sup>-</sup> pathological features (Supplementary Figure S1E). Notably, in vivo treatment revealed that KP-ICC tumors exhibited resistance to GP chemotherapy (gemcitabine and cisplatin), immunotherapy (anti-PD-L1 antibody), and their combination (Figure 1A, Supplementary Figure S1F-G), thereby highlighting KP-ICC as an ideal model for exploring CIT sensitization strategies of ICC.

To uncover metabolic mediators of CIT resistance, we conducted a loss-of-function screen under CIT pressure (in vivo CIT screen) using a murine sgRNA library targeting 2,865 metabolic genes (Figure 1B). Transduced KP-ICC cells (approximately 500-fold sgRNA coverage) were transplanted into mice and treated with placebo, GP, anti-PD-L1, or CIT (GP + anti-PD-L1). Tumors were analyzed after 2 weeks, and MAGECK was used to identify resistance-associated genes across treatment groups (Supplementary Figure S2A, Supplementary Tables S5-S6). The analysis identified several known genes associated with resistance to chemotherapy or immunotherapy, supporting the reliability of the screening results. For example, diacylglycerol kinase alpha and calcium-transporting ATPase type 2C member 2 were linked to resistance to programmed cell death protein 1 (PD-1) blockade and chemotherapy, consistent with previous studies [52–54]. Notably, depletion of gamma-aminobutyric acid receptor subunit theta (GABRQ) enhanced CIT sensitivity, highlighting a potential role for gamma-aminobutyric acid signaling in immune suppression during combination therapy [55].

ratio  $> 1.5$ . (D) Schematic representation for the identification of potential ferroptosis-associated modulators contributing to CIT resistance. (E) Longitudinal monitoring of tumor growth in mice implanted with KP-ICC cells expressing Scr, *shPck1 #1*, or *shPck1 #2*. All mice received CIT treatment (GP + anti-PD-L1). (*n* = 5 per group). (F) Longitudinal monitoring of tumor growth in mice implanted with KP-ICC cells expressing Scr or *shPck1 #1*. Tumor-bearing mice were divided into 4 groups and treated with Placebo, GP, anti-PD-L1, or CIT for 2 weeks (*n* = 5 per group). (G) Assessment of relative lipid peroxidation and cell death in KP-ICC cells expressing Scr, *shPck1 #1* and *shPck1 #2* at 36 h after treatment with GP. (H) Relative lipid peroxidation and cell death were assessed in OVA-overexpressing KP-ICC cells (Scr, *shPck1 #1*, and *shPck1 #2*) after 36 h of incubation with OT-I T cells at a 1:1 effector-to-target ratio (*n* = 3 per group). All data are mean  $\pm$  SD. Statistical significance was determined using 2-way ANOVA for multiple group comparisons and unpaired 2-tailed t-tests for comparisons between 2 groups. \* *P* < 0.05; \*\* *P* < 0.01; \*\*\* *P* < 0.001; ns, not significant.

Abbreviations: GP, gemcitabine + cisplatin; anti-mPD-L1, anti-mouse programmed death-ligand 1; CIT, chemo-immunotherapy (gemcitabine + cisplatin + anti-mPD-L1 antibody); NGS, next-generation sequencing; CRISPR, clustered regularly interspaced short palindromic repeats; sgRNA, single-guide RNA; gDNA, genome DNA; MAGECK, model-based analysis of genome-wide CRISPR-Cas9 knockout; MLE, maximum likelihood estimation; Pck1, phosphoenolpyruvate carboxykinase 1; Scr, scramble shRNA; shRNA, short hairpin RNA; OVA, ovalbumin.

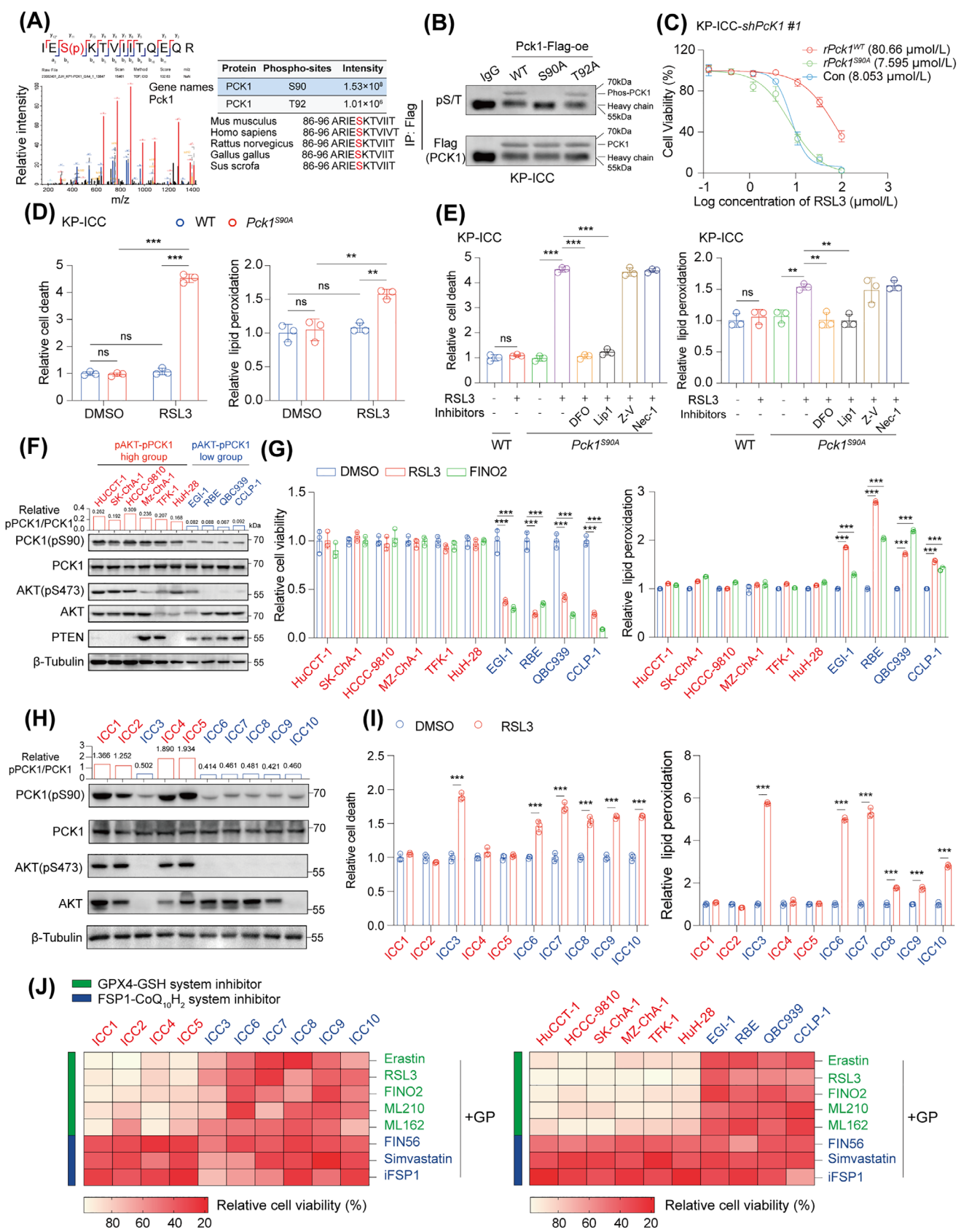


**FIGURE 2** Role of phosphorylated PCK1 in conferring ferroptosis resistance in ICC. (A) IP-MS in KP-ICC cells using an anti-Pck1 antibody to identify phosphorylation-modified peptides. (B) IP and WB assays were performed on Flag-tagged Pck1<sup>WT</sup>, Pck1<sup>S90A</sup>, and Pck1<sup>T92A</sup> overexpressing KP-ICC cells to validate the phosphorylation of Pck1 at S90 and T92 (pS/T, phospho-serine/threonine). (C) IC50 curves of the given cell lines treated with RSL3. (D) Quantitative analysis of lipid peroxidation and cell death was performed in HuCCT-1 WT and PCK1<sup>S90A</sup>

To identify genes with additive effect in CIT, we focused on those with increased effects on CIT compared to that in monotherapies (GP or anti-mPD-L1 antibody). Genes exhibiting an additive score ratio > 1.5 in CIT vs. monotherapy groups included PCK1, endothelin 2, GABRQ, 3'-phosphoadenosine 5'-phosphosulfate synthase 1 (PAPSS1), and fatty acid desaturase 2 (Figure 1C). Considering the immunogenic role of ferroptosis in therapy resistance [5–7], we screened ferroptosis regulators in KP-ICC cells using RSL3 (a commonly used ferroptosis inducer) (Supplementary Figure S2B–C) and integrated the results with the in vivo CIT screen data. This analysis indicated that PCK1 and PAPSS1 were the primary candidates mediating ferroptosis resistance and CIT resistance (Figure 1D).

In the aforementioned analyses, PCK1 played a more significant role compared to PAPSS1 in regulating both CIT and ferroptosis resistance. Based on this finding and the previously established role of PCK1 in tumors from our studies and those of our collaborators [56–58], we further assessed its effect on CIT. In vivo experiments demonstrated that the suppression of PCK1 significantly reduced tumor growth in both BALB/c nude and C57BL/6J mice (Supplementary Figure S2D–E). This effect was further enhanced by the administration of CIT (Figure 1E–F), highlighting PCK1 as both oncogene and primary regulator of CIT resistance in the KP-ICC model.

Additionally, using various human and murine ICC cell lines and PDOs, we demonstrated that chemotherapy (GP)-induced impairment of cell viability could be reversed by the ferroptosis inhibitor Lip1 (Supplementary Figure S3A). The depletion of PCK1 further sensitized ICC cells to GP-induced ferroptosis (Figure 1G, Supplementary Figure S3B–G). Moreover, T cell-specific killing assays revealed that PCK1 depletion enhanced T cell-induced fer-

roptosis, as confirmed by OT-1 T cells co-cultured with OVA-oe KP-ICC cells (Figure 1H) and anti-hHER2 CAR-T cells co-cultured with the HER2-expressing human ICC cell line, HuCCT-1 (Supplementary Figure S3H).

### 3.2 | Phosphorylated PCK1 conferred ferroptosis resistance in ICC

Traditionally regarded as tumor suppressors, gluconeogenic enzymes exhibited complex and context-dependent roles [59]. Recent studies have identified PCK1 as a context-dependent oncogene [40, 58, 60]. In KP-ICC cells, characterized by hyperactive PI3K-AKT and KRAS-activated protein kinase signaling pathways (Supplementary Figure S1D), we hypothesized that PCK1 promoted CIT resistance and ferroptosis resistance through its kinase activity.

To assess this, we performed IP-MS, which revealed 2 phosphorylation sites on PCK1—S90 and T92 (Figure 2A). Notably, the phosphorylation of PCK1 S90 acts as a switch that converts PCK1 from a gluconeogenic enzyme to a protein kinase [40]. Consistently, our IP assays confirmed that S90 was the predominant phosphorylation site in KP-ICC cells (Figure 2B), indicating the presence of an active kinase form of PCK1 in this context.

Using prime editing, we mutated PCK1 at S90 to alanine (mimicking phosphorylation deficiency) or aspartic acid (mimicking phosphorylation) in HuCCT-1 and KP-ICC cells (Supplementary Figure S4A). Subsequent experiments demonstrated that both the elimination of PCK1 S90 phosphorylation and PCK1 knockdown enhanced tumor cell sensitivity to the ferroptosis inducer, RSL3 (Figure 2C–D). This effect was reversed by ferroptosis

HuCCT-1 cells after 36 h of treatment with 10  $\mu\text{mol/L}$  RSL3 ( $n = 3$  per group). (E) Quantitative analysis of lipid peroxidation and cell death was performed in the given ICC cell lines after 36 h of 10  $\mu\text{mol/L}$  RSL3 treatment with or without pre-treatment of specific cell death inhibitors: DFO (ferroptosis inhibitor, 5  $\mu\text{mol/L}$ ), Lip1 (ferroptosis inhibitor, 300 nmol/L), Z-V (apoptosis inhibitor, 10  $\mu\text{mol/L}$ ), and Nec-1 (necroptosis inhibitor, 2  $\mu\text{mol/L}$ ), administered 1 h before RSL3 treatment. (F) To measure pAKT and pPCK1 activation levels in the given CCA cell lines (ICC/ECC), WB was performed on the indicated proteins, and the ratio of PCK1(pS90) to total PCK1 levels was determined. (G) Quantitative analysis of lipid peroxidation and cell viability was performed in the given CCA cell lines treated with 10  $\mu\text{mol/L}$  RSL3 or 10  $\mu\text{mol/L}$  FINO2 (a ferroptosis inducer) for 36 h. (H) WB was performed to assess pAKT-pPCK1 activation-related markers in 10 ICC-PDOs, and the ratio of PCK1(pS90) to total PCK1 levels was determined. (I) Quantitative analysis of lipid peroxidation and cell death was performed in 10 ICC-PDOs treated with 10  $\mu\text{mol/L}$  RSL3 for 36 h. (J) Heatmap of cell viability assays in ICC-PDOs (left panel)/ CCA cell lines (right panel) treated with GP (5 nmol/L gemcitabine and 1  $\mu\text{mol/L}$  cisplatin) with specific ferroptosis inducers: Erastin (10  $\mu\text{mol/L}$ ), RSL3 (10  $\mu\text{mol/L}$ ), FINO2 (10  $\mu\text{mol/L}$ ), ML210 (1  $\mu\text{mol/L}$ ), ML162 (10  $\mu\text{mol/L}$ ), FIN56 (10  $\mu\text{mol/L}$ ), Simvastatin (10 nmol/L), and iFSP1 (200 nmol/L). All data are mean  $\pm$  SD. Statistical significance was determined using 2-way ANOVA for multiple group comparisons and unpaired 2-tailed t-tests for comparisons between 2 groups. \*  $P < 0.05$ ; \*\*  $P < 0.01$ ; \*\*\*  $P < 0.001$ ; ns, not significant.

Abbreviations: IP-MS, immunoprecipitation followed by mass spectrometry; IC50, half maximal inhibitory concentration; ICC, intrahepatic cholangiocarcinoma; ECC, extrahepatic cholangiocarcinoma; CCA, cholangiocarcinoma; PDO, patient-derived organoid; DFO, deferoxamine; Lip1, liproxstatin-1; Z-V, Z-VAD-FMK; Nec-1, necrostatin-1s; PCK1, phosphoenolpyruvate carboxykinase 1; AKT, protein kinase B; PTEN, phosphatase and tensin homolog; GPX4, glutathione peroxidase 4; GSH, glutathione; FSP1, ferroptosis suppressor protein 1; CoQ<sub>10</sub>H<sub>2</sub>, reduced coenzyme Q<sub>10</sub> (Ubiquinol).

inhibitors (DFO and Lip1) but not by apoptosis or necroptosis inhibitors (Figure 2E), implicating the protein-kinase activity of PCK1 promoted ferroptosis resistance in KP-ICC cells.

Subsequently, we generated a phosphorylation-specific antibody against PCK1 S90 (anti-PCK1 pS90) that specifically recognizes PCK1 pS90, as confirmed by IHC in the presence or absence of a PCK1(pS90) blocking peptide (Supplementary Figure S4B). Further assessment explored the relationship between PCK1 kinase activity and PI3K-AKT pathway activation in 10 cholangiocarcinoma [CCA, including 7 ICC and 3 extrahepatic cholangiocarcinoma (ECC)] cell lines and 10 ICC-PDOs (Supplementary Figure S4C). Following analyses demonstrated that cells and PDOs with increased phosphorylated AKT (pAKT)-pPCK1 levels were resistant to RSL3 and FINO2 (Figures 2F-I, Supplementary Figure S4D, Supplementary Table S7), both of which act as GPX4 inhibitors [61]. To further assess therapeutic responses, we screened ferroptosis inducers with distinct mechanisms in these ICC cells, specifically targeting the GPX4-glutathione (GSH) system and the FSP1-CoQ<sub>10</sub>H<sub>2</sub> system. The results demonstrated that PDOs and cells with increased pAKT-pPCK1 levels exhibited enhanced responses to GP in combination with a series of FSP1-CoQ<sub>10</sub>H<sub>2</sub> system inhibitors but not to GP with GPX4-GSH system inhibitors (Figure 2J). These findings indicated that PCK1 kinase activity contributed to ferroptosis resistance in AKT-hyperactivated ICC cells through a different surveillance mechanism that depends on the FSP1-CoQ<sub>10</sub>H<sub>2</sub> system rather than the GPX4-GSH system, highlighting the need for further validation.

### 3.3 | PCK1 phosphorylation blockade enhanced CIT efficacy in a ferroptosis-dependent manner

We conducted experiments on various ICC cell lines to assess the role of PCK1 in various activation states of the pAKT-pPCK1 axis. PCK1 depletion increased RSL3-induced ferroptosis susceptibility in cell lines with elevated pAKT-pPCK1 activity (e.g., HuCCT-1 and HCCC-9810), but had no effect in cell lines with lower pAKT-pPCK1 levels (e.g., QBC939 and RBE), which were intrinsically sensitive to RSL3 regardless of PCK1 status (Figure 3A-B, Supplementary Figure S5A). Reintroduction of wild-type PCK1 (PCK1<sup>WT</sup>) restored ferroptosis resistance, whereas the phosphorylation-deficient variant PCK1<sup>S90A</sup> did not (Figure 3C, Supplementary Figure S5B). These results indicated that PCK1 primarily contributes to ferroptosis resistance when pAKT-pPCK1 signaling is active.

Based on these findings, we designed a competitive inhibitory peptide, PPB peptide, to block phosphorylation

at the S90 of PCK1 (Figure 3D). The mechanism of action of PPB involves a PCK1 84-94 peptide, composed of 11 amino acids, located at the AKT-binding and phosphorylation site of PCK1 S90. It competitively binds to AKT, thereby blocking the AKT-mediated phosphorylation of PCK1 at S90. PPB effectively inhibited the interaction between PCK1 and AKT, and PCK1 S90 phosphorylation in vitro (Supplementary Figure S5C-D), resulting in enhanced susceptibility to GP-induced ferroptosis (Figure 3E-F). In vivo, PPB enhanced the therapeutic efficacy of CIT in KP-ICC cells (Figure 3G-K, Supplementary Figure S5E-G). Lip1 administration reversed these effects, highlighting the significance of S90 phosphorylation in PCK1's modulation of ferroptosis and its implications in CIT. These results demonstrated that pPCK1 drives ferroptosis evasion and CIT resistance in ICC.

### 3.4 | 4 pPCK1 mediated lactate metabolism-MVA flux reprogramming driving ferroptosis resistance in ICC

Subsequently, we aimed to elucidate the specific mechanisms involved in pPCK1-mediated ferroptosis resistance. PCK1 has a dual function—it regulates gluconeogenesis as a key enzyme and play as a protein kinase that facilitating lipogenesis under AKT hyperactivation [62] (Figure 4A). To elucidate how PCK1 modulates ferroptosis evasion, we assessed its effects on glycolysis and lipogenesis.

Subsequent analysis revealed that pPCK1 reduced its PEPCK enzyme activity (converting oxaloacetate to phosphoenolpyruvate using GTP) (Supplementary Figure S6A). PCK1 depletion reduced glucose uptake, lactate production, and lysine lactylation levels of whole proteins (pan-Klac) in pAKT-pPCK1-high ICC cells (Figure 4B-C, Supplementary Figure S6B-D). In contrast, cells with low pAKT-pPCK1 activity exhibited the opposite effect. Notably, PCK1 depletion did not affect PEPCK enzyme activity in pAKT-pPCK1-high cells (Figure 4D). Furthermore, compared to pAKT-pPCK1-low cells, pAKT-pPCK1-high cells consistently displayed lower PEPCK enzyme activity, indicating that PCK1 in pAKT-pPCK1-high cells do not function as a key enzyme in gluconeogenesis. Therefore, PCK1 appears to facilitate glycolysis via a mechanism independent of its PEPCK enzyme activity under high pAKT-pPCK1 conditions, while primarily supporting gluconeogenesis when pAKT-pPCK1 activity is low.

Additionally, ICC cells harboring the S90A mutation exhibited reduced glycolytic activity compared to wild-type cells in both KP-ICC and HuCCT-1 (pAKT-pPCK1-high) (Supplementary Figure S6E-F). Moreover, we assessed the anti-ferroptotic effects of the primary glycolytic substrates (glucose, pyruvate, and lactate).

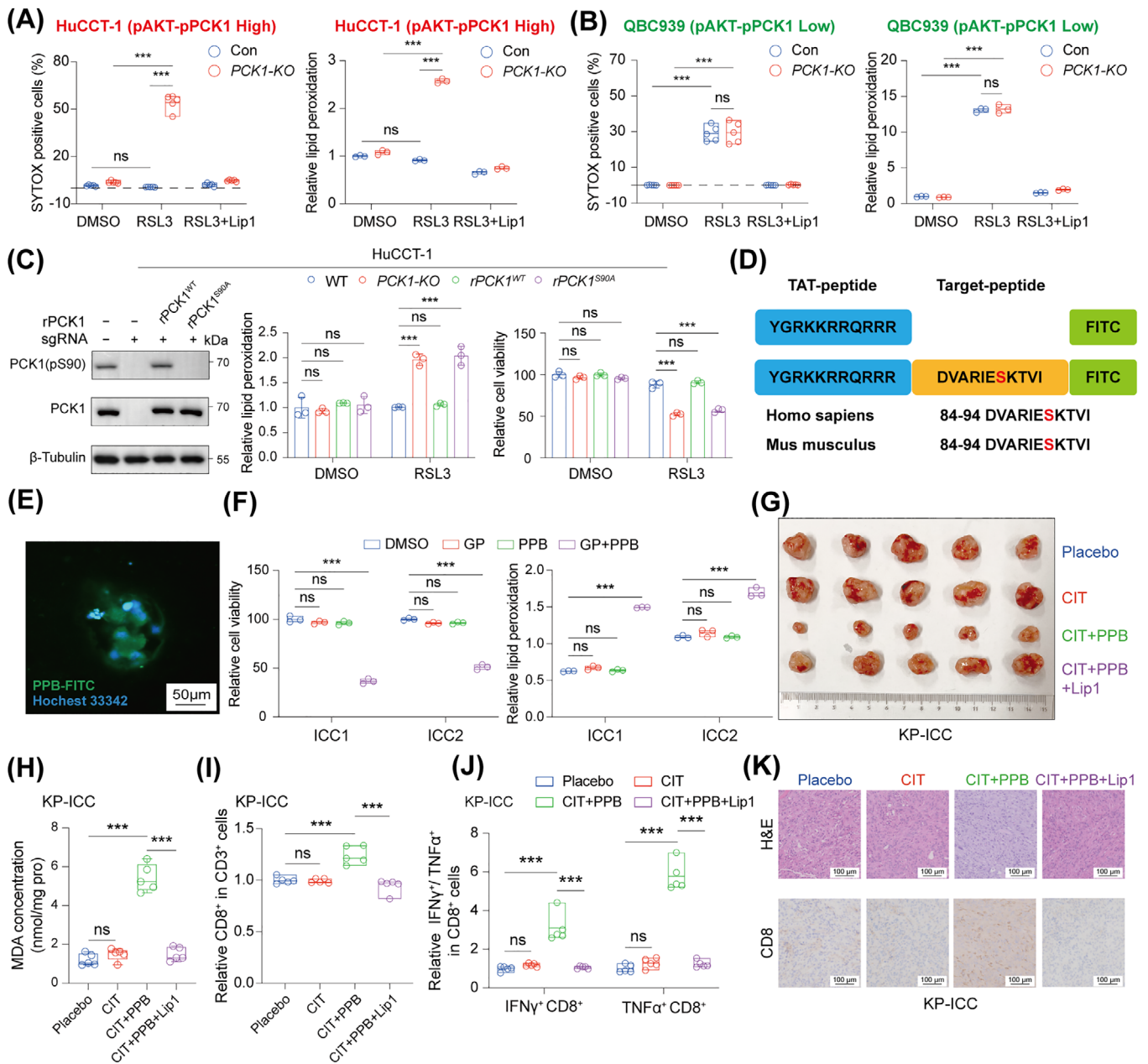


**FIGURE 3** Inhibition of PCK1 phosphorylation augments CIT efficacy through ferroptosis. (A-B) Cell death and lipid peroxidation were measured in HuCCT-1 and QBC939 cells (Con and *PCK1*-KO) treated with RSL3 (10 µmol/L) for 36 h, with or without 1 h pre-treatment with Lip1 (300 nmol/L). (C) WB probed specific proteins in HuCCT-1 cells (left); measurement of cell viability and lipid peroxidation in the given cells 36 h post 10 µmol/L RSL3 treatment (right). (D) Schematic representation of the TAT-PPB peptide sequence. (E) Representative fluorescence microscopy images of ICC-PDO treated with TAT-PPB peptides (1 µg/mL). (F) Measurement of cell viability (left) and lipid peroxidation (right) in pAKT-pPCK1 high ICC-PDOs (ICC1 and ICC2) 36 h post treatment with GP and PPB (1 µg/mL). (G-K) KP-ICC cells were subcutaneously injected into C57BL/6J mice. One-week post subcutaneous injection, mice received 2 weeks of indicated treatments. Subsequent analysis included: tumor general over view (G), intratumoral MDA concentrations (for lipid peroxidation evaluation) (H), CD3<sup>+</sup>CD8<sup>+</sup> T cell percentages (I), TNF $\alpha$ <sup>+</sup>/IFN $\gamma$ <sup>+</sup> CD8<sup>+</sup> T cell percentages (J) and IHC analysis for CD8<sup>+</sup> T cell infiltration (K). All data are mean  $\pm$  SD. Statistical significance was determined using 2-way ANOVA for multiple group comparisons and unpaired 2-tailed t-tests for comparisons between 2 groups. \*  $P < 0.05$ ; \*\*  $P < 0.01$ ; \*\*\*  $P < 0.001$ ; ns, not significant.

Abbreviations: Con, control; WT, wild type; KO, knockout; rPCK1, *PCK1*-KO + recombinant PCK1 overexpression; PCK1, phosphoenolpyruvate carboxykinase 1; Lip-1, liprostatin-1; CIT, chemo-immunotherapy; TAT, trans-activator of transcription; PPB, PCK1 phosphorylation blocker; ICC, intrahepatic cholangiocarcinoma; PDO, patient-derived organoid; MDA, malondialdehyde; IFN $\gamma$ , interferon gamma; TNF $\alpha$ , tumor necrosis factor alpha.

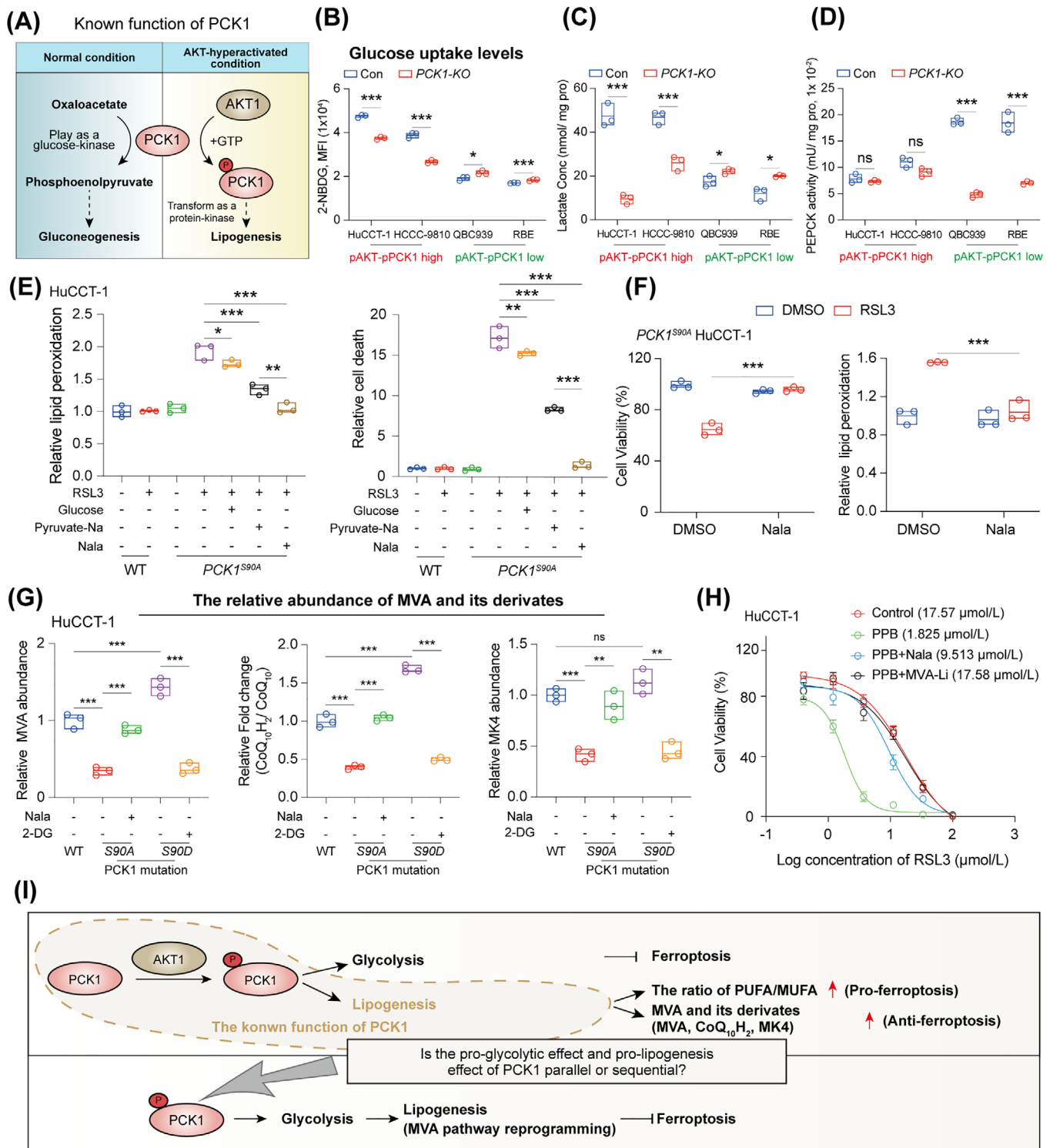


**FIGURE 4** pPCK1 modulates lactate metabolism-mevalonate flux reprogramming, contributing to ferroptosis resistance in ICC. (A) The scheme summarizes the known function of PCK1. (B-D) Assessment of glucose uptake (B), intracellular lactate concentrations (C), and PEPCK enzyme activity (D) in ICC cell lines with high pAKT-pPCK1 activation (HuCCT-1, HCCC-9810) and low pAKT-pPCK1 activation (QBC939, RBE), with or without PCK1 knockout. (E) Measurements of lipid peroxidation and cell death in HuCCT-1-WT or *PCK1*<sup>S90A</sup> HuCCT-1 after 36 h of indicated treatments (10 mmol/L glucose; 10 mmol/L Pyruvate-Na; 10 mmol/L Nala), followed by exposure to 10 μmol/L RSL3 for an additional 36 h. (F) Measurements of lipid peroxidation and cell viability in *PCK1*<sup>S90A</sup> HuCCT with 36 h of Nala treatments, followed by exposure to RSL3 for an additional 36 h. (G) Detection of intermediate metabolites in the MVA pathway (MVA, CoQ<sub>10</sub>H<sub>2</sub>, MK4) in HuCCT-1-WT/*PCK1*<sup>S90A</sup> HuCCT-1/*PCK1*<sup>S90D</sup> HuCCT-1, with and without administration of Nala or 10 mmol/L 2-DG for 24 h. (H) IC<sub>50</sub> curves for HuCCT-1 cells under indicated treatments (1 μg/mL PPB; 10 mmol/L Nala; 500 μmol/L MVA-Li). (I) The scheme summarizes the findings. Briefly, in AKT-hyperactivated ICC, AKT phosphorylates PCK1 at Ser90, driving metabolic reprogramming

These results indicated that lactate reduced ferroptosis sensitivity because of the inactivation of pPCK1, pyruvate had a moderate effect, and glucose had a minimal effect (Figure 4E). Supplementation with Nala restored ferroptosis sensitivity caused by the inactivation of pPCK1 (Figure 4F), and the glycolysis inhibitor 2-DG showed opposite effect (Supplementary Figure S6G). Assessment of lipogenesis revealed that pPCK1 significantly enhanced lipid metabolic processes. Specifically, pPCK1 promoted the production of mature SREBPs (n-SREBPs) (Supplementary Figure S6H) and increased the transcriptional activity of SRE (Supplementary Figure S6I), consistent with previous reports on the kinase function of PCK1 [40]. Our attention subsequently shifted to investigating the role of pPCK1's pro-glycolytic and pro-lipogenic effects in mediating ferroptosis resistance.

The anti-ferroptotic activity governed by lipogenesis primarily involves SREBP1-mediated MUFA synthesis and SREBP2-mediated MVA pathway reprogramming, facilitating the synthesis of radical-trapping antioxidants, such as CoQ<sub>10</sub>H<sub>2</sub> and MK4 [13, 63] (Supplementary Figure S6J). Lipidomics analysis demonstrated that pPCK1 facilitated the production of both PUFA and saturated fatty acids, with MUFA unaffected, resulting in an elevated PUFA-to-MUFA ratio (Supplementary Figure S6K, Supplementary Table S8). This ratio provides more substrates for lipid peroxidation and, therefore, cannot explain the anti-ferroptotic effect of pPCK1. In parallel, pPCK1 significantly facilitated the synthesis of MVA and its downstream products, CoQ<sub>10</sub>H<sub>2</sub> and MK4; inhibition of glycolysis using 2-DG significantly reduced pPCK1-mediated lipogenesis and the synthesis of MVA and its derivatives (CoQ<sub>10</sub>H<sub>2</sub> and MK4) (Figure 4G, Supplementary Figure S7A). Supplementation with Nala or MVA-Li significantly restored ferroptosis sensitization caused by pPCK1 deficiency both in vitro (RSL3 as the in vitro ferroptosis inducer) and in vivo (IKE as the in vivo ferroptosis inducer) (Figure 4H, Supplementary Figure S7B-F). Further in vivo rescue assays demonstrated that supplementation with Nala and MVA-Li effectively reversed ferroptosis sensitization induced by PCK1 phosphorylation or glycolysis inhibition. However, when the MVA pathway was inhibited, MVA-Li supplementation successfully restored ferroptosis resistance, whereas Nala could not (Supplementary Figure S7G-J).

In summary, these data indicate that the pro-glycolytic and pro-lipogenic effects mediated by pPCK1 (via SREBP2-driven MVA flux) occur sequentially. pPCK1 plays a critical role in linking glycolysis to the MVA pathway, thereby enabling ICC cells to evade ferroptosis (Figure 4I). This finding also partially explained the observation in Figure 2J that tumors with high pAKT-pPCK1 levels were more sensitive to FSP1-CoQ<sub>10</sub>H<sub>2</sub> system-related ferroptosis inducers, highlighting the complex interplay between PCK1 S90 phosphorylation and SREBP2-driven MVA flux.

### 3.5 | 5 pPCK1-pLDHA axis facilitated lactate metabolism-MVA flux reprogramming in ICC

Next, we aimed to explore the specific mechanism through which pPCK1 promotes glycolysis. Using IP-MS, we identified protein interactions unique to PCK1<sup>WT</sup> and PCK1<sup>S90A</sup>, notably with LDHA (Figure 5A, Supplementary Table S9). The analysis highlighted T248 as an important phosphorylation site on LDHA that is important for its enzyme activity, as confirmed by point-mutation experiments and in vitro enzyme activity assays (Figure 5B-C).

To further investigate the role of LDHA (pT248) in pPCK1-mediated lactate metabolism-MVA flux reprogramming, we developed a custom antibody targeting the LDHA (pT248) site and validated its specificity (Supplementary Figure S8A). Further analysis revealed that PCK1 overexpression increased LDHA (pT248) and pan-Klac levels in HuCCT-1 and HCCC-9810 cells, while the total protein levels of LDHA remained unchanged regardless of its phosphorylation status (Supplementary Figure S8B). Insulin-like growth factor 1 (IGF-1) stimulation—that enhances AKT activation [40]—enhanced PCK1-LDHA interactions in PCK1<sup>WT</sup>-expressing cells but not in PCK1<sup>S90A</sup> variants, and LDHA phosphorylation at T248 was enhanced in PCK1<sup>WT</sup> cells upon IGF-1 exposure (Supplementary Figure S8C). Confocal microscopy analysis demonstrated that PCK1<sup>S90A</sup> disrupted the colocalization of PCK1 and LDHA (Figure 5D). In vitro protein pulldown and kinase assays demonstrated that the PCK1-LDHA interaction was mediated by AKT-directed PCK1 S90 phosphorylation (Figure 5E); pPCK1 directly bound

(enhanced glycolysis/lipogenesis) and ferroptosis resistance. Mechanistically, pPCK1 activates the mevalonate pathway by enhancing glycolysis, boosting synthesis of radical-scavenging antioxidants (CoQ<sub>10</sub>H<sub>2</sub>, MK4), thereby shielding cells from ferroptosis. All data are mean ± SD. Statistical significance was determined using 2-way ANOVA for multiple group comparisons and unpaired 2-tailed t-tests for comparisons between 2 groups. \* *P* < 0.05; \*\* *P* < 0.01; \*\*\* *P* < 0.001; ns, not significant.

Abbreviations: 2-NBDG, 2-(n-(7-nitrobenz-2-oxa-1,3-diazol-4-yl) amino)-2-deoxyglucose; PEPCK, phosphoenolpyruvate carboxykinase; Pyruvate-Na, sodium pyruvate; PUFA, polyunsaturated fatty acid; MUFA, monounsaturated fatty acid; MVA, mevalonate; MVA-Li, mevalonic acid lithium salt; CoQ<sub>10</sub>H<sub>2</sub>, reduced coenzyme Q<sub>10</sub> (Ubiquinol); MK4, menaquinone-4; Nala, sodium L-lactate; 2-DG, 2-deoxyglucose.

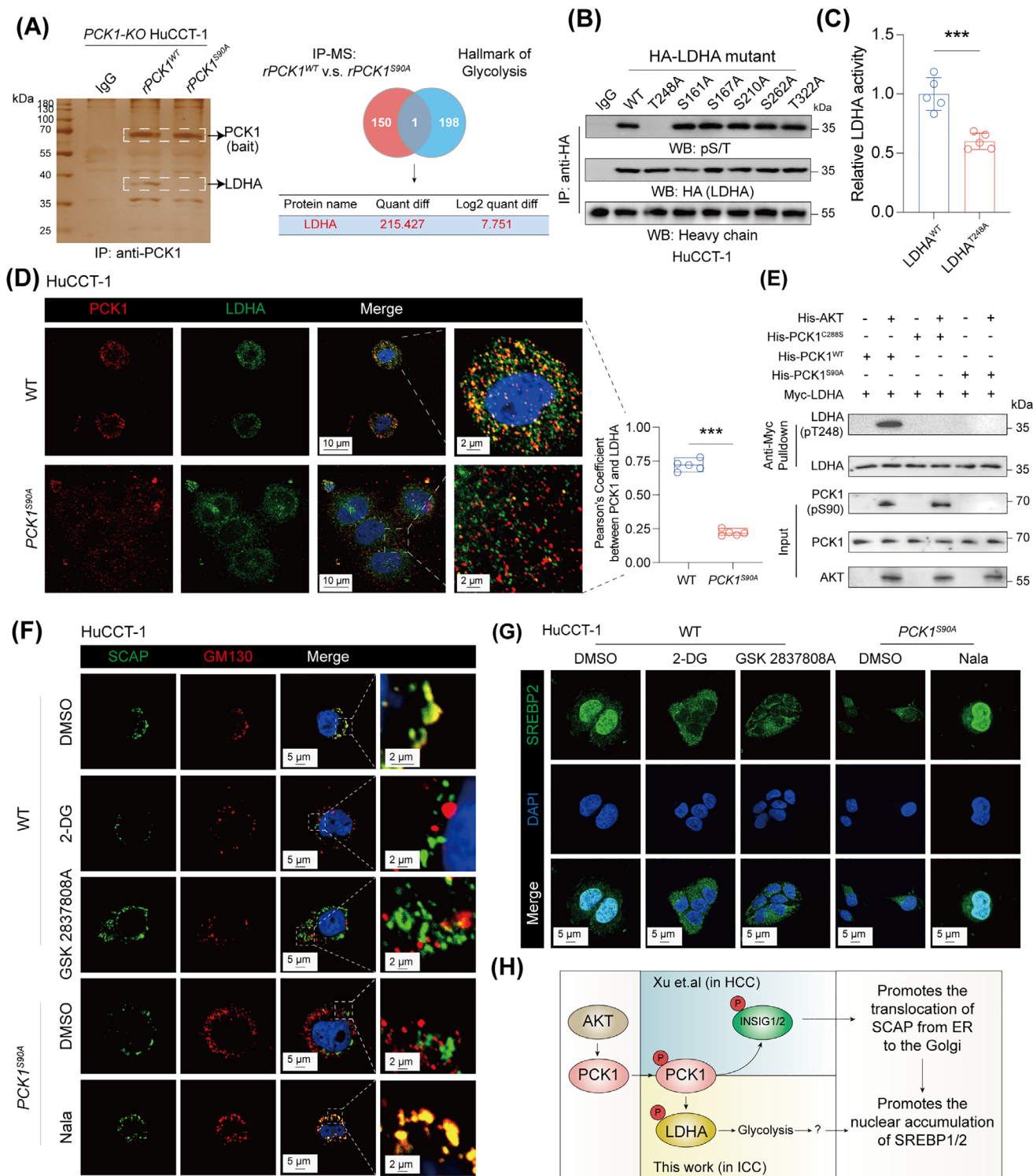


**FIGURE 5** The pPCK1-pLDHA axis promotes the translocation of SCAP, thereby facilitating MVA flux reprogramming in ICC. (A) IP assays conducted in *PCK1*-KO HuCCT-1 cells re-expressing *PCK1*<sup>WT</sup> (rPCK1<sup>WT</sup>) or *PCK1*<sup>S90A</sup> (rPCK1<sup>S90A</sup>) using anti-PCK1 antibody. The precipitated PCK1-binding peptides were resolved by SDS-PAGE and visualized with silver stain. Notable peptide hits associated with PCK1 identified via IP-MS are indicated. (B) Potential phosphorylation sites on LDHA were identified using SCANSITE and PhosphoSite analysis. Wild-type LDHA (LDHA<sup>WT</sup>) and its indicated mutation were overexpressed in HuCCT-1 cells, followed by IP with anti-HA antibody and subsequent WB analysis. (C) HEK-293T cells expressing His-LDHA<sup>WT</sup> or His-LDHA<sup>T248A</sup> were purified, and LDHA enzyme activity was detected. (D) Representative immunofluorescence colocalization studies were performed to assess the colocalization of PCK1 and LDHA in specified ICC cells. Pearson's coefficients between PCK1 and LDHA in each group were presented. (E) In vitro kinase assay of purified recombinant His-tagged PCK1<sup>WT</sup>, His-PCK1<sup>S90A</sup>, or His-PCK1<sup>C288S</sup> with active His-AKT in the presence of ATP, followed by interaction assays with Myc-tagged LDHA in the presence of GTP. (F) Representative immunofluorescence images of the localization of SCAP (green), GM130

and phosphorylated LDHA at T248 (Supplementary Figure S8D-E). The specificity of the PCK1-LDHA interaction was confirmed by purifying the phosphorylated and non-phosphorylated PCK1 obtained from HuCCT-1 cells with or without IGF-1 stimulation (Supplementary Figure S8F). The PPB peptide disrupted the PCK1-LDHA interaction regardless of IGF-1 stimulation (Supplementary Figure S8G), further confirming its blocking efficacy in pPCK1-pLDHA interaction.

Additionally, the administration of 2-DG or the LDHA-specific inhibitor GSK 2837808A significantly reduced the translocation of SCAP from the endoplasmic reticulum (ER) to the Golgi and nuclear accumulation of SREBP2, and supplementation with Nala shown the opposite effects (Figure 5F-G; Supplementary Figure S8H-J). In HCC, pPCK1 facilitates SCAP-SREBP complex translocation by directly binding to insulin-induced genes [40], but this interaction was not observed in ICC cells (Supplementary Figure S8K-L). Additionally, overexpression of LDHA<sup>WT</sup> fully rescued the pro-glycolytic and MVA pathway reprogramming abilities in LDHA pT248-deficient cells, whereas re-overexpression of LDHA<sup>T248A</sup> only partially rescued these abilities (Supplementary Figure S9), indicating that the T248 site on LDHA is important for its function.

In summary, these results indicated that pPCK1 facilitates glycolysis by directly binding and phosphorylating LDHA at T248, thereby affecting SCAP-SREBP complex translocation through unknown mechanisms. This reprograms the MVA pathway (Figure 5H), thereby enabling ferroptosis evasion in ICC cells.

### 3.6 | KAT7-mediated SPRING K82 lactylation regulated the pPCK1-pLDHA axis-mediated anti-ferroptotic effects

In the previous section, we discussed how the pPCK1-pLDHA axis reprograms lactate metabolism and MVA flux,

contributing to ICC cell resistance to ferroptosis. This pathway modulates SCAP translocation, activating MVA flux, though the mechanism by which it regulates SCAP translocation to the Golgi remains unclear. The focus on lactylation connecting glycolysis to biological processes resulted in the hypothesis that the pPCK1-pLDHA axis may control SCAP translocation through lactylation [64–66]. IP assays using a pan-Klac antibody identified lactylated peptides in HuCCT-1-WT and PCK1<sup>S90A</sup> HuCCT-1 cells (Figure 6A, Supplementary Table S10). IP-MS analysis revealed the enrichment of lactylated SPRING peptides at K82 in WT cells but not in PCK1<sup>S90A</sup> cells. SPRING is a newly identified protein that regulates hepatic SREBP signaling and aids lipid metabolism by facilitating SCAP movement from the Golgi to the ER, thereby increasing SCAP availability for transporting SREBPs to the Golgi [67–70]. The alignment of SPRING's role with the pro-lipogenic effects of the pPCK1-pLDHA axis, particularly in SCAP Golgi translocation, underscores the mechanistic role of lactylated SPRING, mediated by the pPCK1-pLDHA axis, in promoting the retrograde flow of SCAP from the Golgi to the ER, thereby enhancing SCAP-SREBP transport efficiency.

The significance of SPRING K82 conservation is highlighted by its presence in different species (Figure 6B). Overexpression of SPRING<sup>K82R</sup> (mimicking lactylation deficiency) eliminated SPRING lactylation (Figure 6C), decreased the SREBP1/2 maturation, and was unresponsive to Nala stimulation (Figure 6D). Meanwhile, glycolysis and LDHA inhibition eliminated SPRING lactylation (Figure 6E). Furthermore, we utilized prime editing to generate genome-engineered SPRING<sup>K82R</sup> mutation in HuCCT-1 and KP-ICC cells (Supplementary Figure S10A). This alteration reduced the expression of genes involved in lipid metabolism, SRE transcriptional activation, and SREBP1/2 maturation (Figure 6F, Supplementary Figure S10B-E) and significantly sensitized pAKT-pPCK1-high ICC cells to ferroptosis inducers (Figure 6G). Additionally, SPRING<sup>K82R</sup> mutation significantly downregulated MVA flux (Supplementary Figure S10F). Moreover, blocking

(Golgi marker, red), and nuclei (DAPI, blue) in HuCCT-1-WT or PCK1<sup>S90A</sup> HuCCT-1 after the indicated treatments for 36 h. Treatments included 10 mmol/L 2-DG; 10 nmol/L GSK 2837808A (specific LDHA inhibitor); 10 mmol/L Nala. (G) Representative immunofluorescence images showing SREBP2 (green) localization in the nucleus (DAPI, blue) in HuCCT-1-WT or PCK1<sup>S90A</sup> HuCCT-1 after the indicated treatments. (H) The scheme summarizes the findings. Xu et al. found that in AKT-hyperactivated HCC, pPCK1 promotes SCAP translocation from the ER to the Golgi by binding and phosphorylating INSIGs. However, our work found that in AKT-hyperactivated ICC, pPCK1 cannot bind to INSIGs but can still regulate SCAP translocation by directly binding and phosphorylating LDHA at T248 in a lactate-dependent manner. All data are mean ± SD. Statistical significance was determined using 2-way ANOVA for multiple group comparisons and unpaired 2-tailed t-tests for comparisons between 2 groups. \*  $P < 0.05$ ; \*\*  $P < 0.01$ ; \*\*\*  $P < 0.001$ ; ns, not significant.

Abbreviations: IP, immunoprecipitation; rPCK1<sup>WT/S90A/S90D</sup>, PCK1-KO+recombinant PCK1<sup>WT/S90A/S90D</sup> overexpression; PCK1, phosphoenolpyruvate carboxykinase 1; LDHA, lactate dehydrogenase A; WT, wild type; SCAP, SREBP cleavage activating protein; GM130, golgi matrix protein of 130 kDa; Nala, sodium L-lactate; 2-DG, 2-deoxyglucose; SREBP2, sterol regulatory element-binding protein 2; AKT, protein kinase B; INSIG1/2, insulin induced gene 1/2; ER, endoplasmic reticulum.

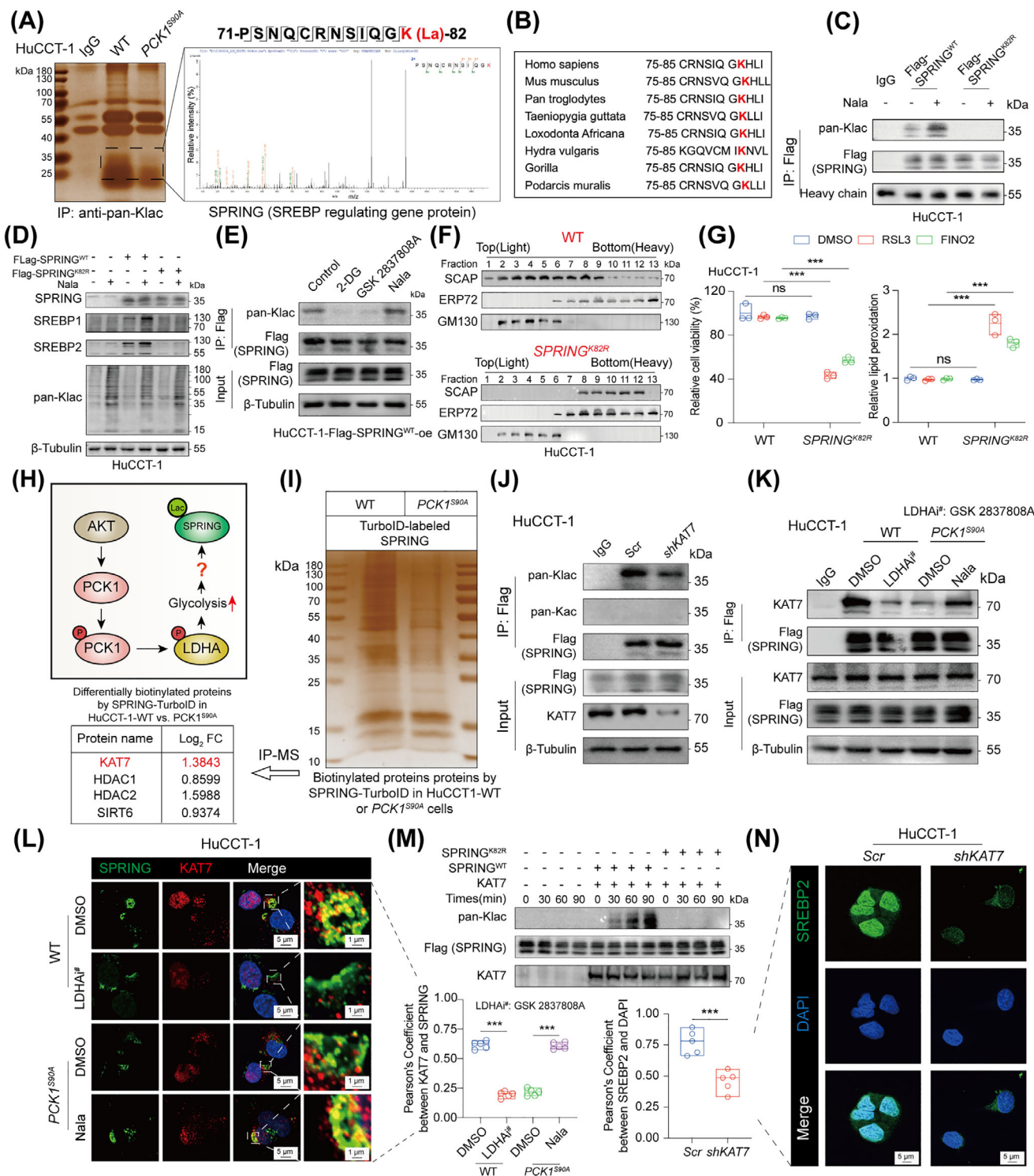


**FIGURE 6** Lactylation by KAT7 at SPRING's K82 is essential for pPCK1-pLDHA axis and its anti-ferroptotic role. (A) IP assays were performed in HuCCT-1-WT and *PCK1<sup>S90A</sup>* HuCCT-1 using an anti-pan-Klac antibody. Peptides with lysine lactylation modifications were separated by SDS-PAGE, silver-stained, and identified by mass spectrometry. (B) Sequence alignment of SPRINGK82 across species. (C) HuCCT-1 cells with or without Flag-SPRING<sup>WT</sup>/SPRING<sup>K82R</sup> overexpression were treated with 10 mmol/L Nala for 36 h. IP assays by anti-Flag antibody followed by WB measurements was performed on whole-cell lysates. (D) WB measurements of whole-cell lysates from HuCCT-1 cells with or without Flag-SPRING<sup>WT</sup>/SPRING<sup>K82R</sup> overexpression, following treatment with 10 mmol/L Nala for 36 h. (E) IP and WB measurements of HuCCT-1 cells with Flag-SPRING<sup>WT</sup> overexpression after 36 h of indicated treatments (10 mmol/L 2-DG; 10 nmol/L GSK 2837808A; 10 mmol/L Nala). (F) Subcellular fractionation from HuCCT-1-WT and *SPRING<sup>K82R</sup>* HuCCT-1 cells, followed by WB with specific antibodies. (G) Assessment of relative cell viability and lipid peroxidation in HuCCT-1-WT and *SPRING<sup>K82R</sup>* HuCCT-1 under treatment with 10 μmol/L RSL3 or 10 μmol/L FINO2 for 36 h. (H) The scheme summarizes current findings and remaining questions. The

pPCK1 or specific inhibition of LDHA significantly abolished SPRING overexpression-mediated ferroptosis resistance (Supplementary Figure S10G).

For now, this study revealed that SPRING lactylation at K82 positively affects lipid metabolism, providing insights into the SCAP translocation mechanism through the pPCK1-pLDHA axis. However, the process by which the pPCK1-pLDHA axis-generated lactate catalyzes SPRING lactylation at K82 remains unclear (Figure 6H). TurboID was used to identify acyltransferases that interact with SPRING in HuCCT-1 WT and *PCK1<sup>S90A</sup>* cells. TurboID-MS analysis indicated a higher proximity between SPRING and KAT7 in WT cells than that in *PCK1<sup>S90A</sup>* cells (Figure 6I). Further analysis demonstrated that KAT7 inhibition reduced SPRING lactylation without affecting acetylation (Figure 6J), whereas LDHA inhibition reduced the KAT7-SPRING interaction, and Nala administration had the opposite effect (Figure 6K-L). *in vitro* experiments demonstrated the role of KAT7 in lactylating SPRING at K82 (Figure 6M). KAT7 inhibition significantly affected SCAP Golgi translocation and SREBP2 nuclear accumulation (Figure 6N, Supplementary Figure S10H). These results collectively suggest that KAT7-mediated SPRING lactylation serves as a key intermediary in the pPCK1-pLDHA-driven reprogramming of glycolysis and the MVA pathway.

### 3.7 | Therapeutic targeting of pPCK1-pLDHA-SPRINGlac axis with simvastatin sensitized CIT efficacy in ICC

Our analysis highlighted the significance of pPCK1 in regulating ferroptosis and CIT resistance by modulating MVA flux reprogramming. Nala upregulated MVA

pathway genes, an effect countered by the SPRING<sup>K82R</sup> mutation (Figure 7A). Considering the role of statins in the inhibition of 3-hydroxy-3-methylglutaryl-CoA reductase (HMGCR), the rate-limiting enzyme in the MVA pathway [71], we assessed the effect of simvastatin on the pPCK1-pLDHA-SPRINGlac axis. Simvastatin sensitized HuCCT-1 cells to RSL3, which is dependent on the MVA pathway for ferroptosis regulation (Figure 7B). Depletion of CoQ<sub>2</sub> and UBIAD1, the primary enzymes in CoQ<sub>10</sub>H<sub>2</sub> and MK4 synthesis, weakened pPCK1-pLDHA-SPRINGlac-mediated ferroptosis resistance (Supplementary Figure S11A-C), indicating that these derivatives were important for the anti-ferroptotic effects of this cascade.

Subsequent *in vivo* experiments demonstrated that individual treatments with the PPB peptide, simvastatin, or CIT were insufficient to inhibit ICC cell growth; in contrast, combining CIT with PPB peptide or simvastatin significantly reduced tumor growth (Figure 7C-E), increased lipid peroxidation (Figure 7F), and enhanced CD8<sup>+</sup> T cell infiltration (Figure 7G-I). *in vivo* rescue experiments showed that MVA supplementation attenuated the enhanced tumor-killing effect of the CIT and simvastatin combination (Figure 7J-N). To further confirm the additive effect of simvastatin and CIT on AKT-hyperactivated ICC, we used a hydrodynamic tail vein injection-induced murine ICC model expressing the activated forms of AKT (myr-Akt) and Notch1 (Notch intracellular domain) (Supplementary Figure S11D). This model recapitulated the sensitizing effect of simvastatin on CIT, demonstrating significant suppression of tumor growth (Supplementary Figure S11E-G), increased lipid peroxidation (Supplementary Figure S11H), augmented CD8<sup>+</sup> T cell infiltration and activation (Supplementary Figure S11I-J).

In conclusion, our findings supported the clinical feasibility of targeting the MVA pathway with simvastatin

pPCK1-pLDHA axis promotes SCAP translocation and SREBP nuclear accumulation via SPRING K82 lactylation. However, the enzyme responsible for SPRING K82 lactylation remains to be identified despite the lactate accumulation caused by the pPCK1-pLDHA axis. (I) Biotinylated proteins from HuCCT-1-WT and *PCK1<sup>S90A</sup>* HuCCT-1 cells were enriched and analyzed by mass spectrometry. Enrichment results are presented as a silver-stained gel. (J-K) IP and WB analyses of HuCCT-1-Scr or HuCCT-1-*shKAT7* (J) and HuCCT-1-WT/ *PCK1<sup>S90A</sup>* HuCCT-1 cells treated with 10 nmol/L LDHAi (GSK 2837808A) or 10 mmol/L Nala (K). (L) Representative immunofluorescence colocalization studies were performed to evaluate the colocalization of SPRING and KAT7 in specified cells following 36 h of indicated treatments. The Pearson's coefficient between PCK1 and KAT7 was calculated and presented for each group. The treatments included 10 nmol/L GSK 2837808A and 10 mmol/L Nala. (M) An *in vitro* lactylation assay was performed using Flag-SPRING<sup>WT</sup> and Flag-SPRING<sup>K82R</sup> purified from HEK-293T cells, along with KAT7-HA also derived from HEK-293T cells. SPRING lactylation levels were assessed using a pan-Klac antibody. (N) Representative immunofluorescence images and Pearson's coefficient analysis of SREBP2 nuclear localization in HuCCT-Scr and HuCCT-1-*shKAT7*. All data are mean ± SD. Statistical significance was determined using 2-way ANOVA for multiple group comparisons and unpaired 2-tailed t-tests for comparisons between 2 groups. \* *P* < 0.05; \*\* *P* < 0.01; \*\*\* *P* < 0.001; ns, not significant.

Abbreviations: Pan-Klac, pan-lysine lactylation; SPRING, SREBP-regulating gene protein; Nala, sodium-L-lactate; SREBP1/2, sterol regulatory element-binding protein 1; SCAP, SREBP cleavage-activating protein; GM130, golgi matrix protein 130; ERP72, endoplasmic reticulum protein 72; PPB, PCK1 phosphorylation blocker; Lac, lactylation; HDAC1, histone deacetylase 1; HDAC2, histone deacetylase 2; SIRT6, sirtuin 6; AKT, protein kinase B; PCK1, phosphoenolpyruvate carboxykinase 1; LDHA, lactate dehydrogenase A; MVA, mevalonate; CoQ<sub>10</sub>H<sub>2</sub>, reduced coenzyme Q10 (Ubiquinol); MK-4, menaquinone-4 (vitamin K2).

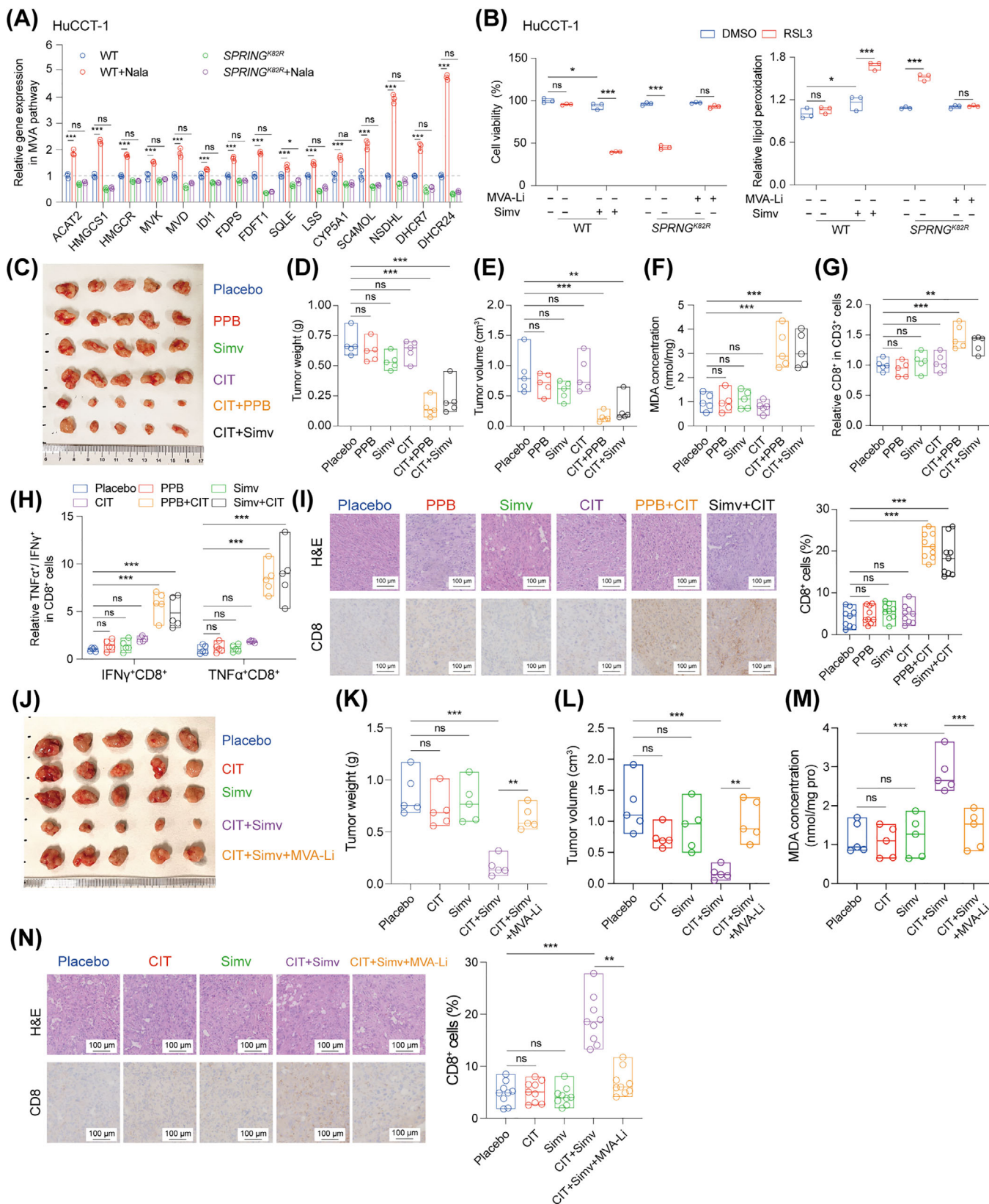


**FIGURE 7** Simvastatin mediates enhanced CIT efficacy in ICC through disruption of the pPCK1-pLDHA-SPRINGlac axis. (A) mRNA expression levels of mevalonate pathway-related genes in HuCCT-1-WT and *SPRING<sup>K82R</sup>* HuCCT-1, treated with or without 10 mmol/L Nala for 36 h. (B) Assessment of cell viability and lipid peroxidation in HuCCT-1-WT and *SPRING<sup>K82R</sup>* HuCCT-1 with or without indicated treatments for 36 h. (C-I) KP-ICC cells were subcutaneously injected into C57BL/6J mice. One week after injection, mice received 2 weeks of the indicated treatments [Placebo, PPB, Simv (simvastatin), CIT, CIT + PPB, CIT + Simv]. Subsequent analyses of KP-ICC tumors included

as an adjunct to sensitizing CIT in patients with AKT-hyperactivated ICC.

### 3.8 | ICC Patients with low levels of PCK1 S90 phosphorylation benefited significantly from CIT

In the previous sections, we highlighted the important role of pPCK1 in mediating CIT resistance, specifically under the conditions of PI3K-AKT hyperactivation. Based on these insights, we assessed the association between the phosphorylation status of PCK1 and prognostic outcomes in patients with ICC subjected to CIT.

Tissue samples from 36 ICC patients treated with CIT prior to surgical resection (the TJH-ICC-CIT cohort) were analyzed to determine the prognostic value of pAKT-pPCK1 levels. The observed objective response rate was 22.2%, with a disease control rate of 47.2% (Figure 8A-B), aligning with the response rates reported in the TOPAZ-1 study (objective response rate, 26.7%; partial response, 24.6%) [3]. Notably, increased pAKT and pPCK1 levels were characteristic features in patients with progressive disease, in contrast to lower levels in those exhibiting partial response or stable disease; survival analyses further substantiated that patient with ICC with reduced AKT S473 and PCK1 S90 phosphorylation levels benefited significantly from the CIT regimen (Figure 8C-D), highlighting the potential of the pAKT-pPCK1 axis as a predictive biomarker for treatment efficacy.

In parallel, IHC analyses were conducted on a tissue microarray-based cohort (the TJH-ICC-TMA-A cohort) of 68 primary ICC samples to explore the correlation among pAKT, pPCK1, and pan-Klac. Additionally, 121 primary ICC samples with follow-up data (from TJH-ICC-TMA-A + TJH-ICC-TMA-B) were used to investigate the clinical significance of pPCK1, 58 cases (from TJH-ICC-TMA-A)

were analyzed for pAKT significance. Significant associations were identified between pAKT, pPCK1 and pan-Klac in the 68 resected ICC tumors (Supplementary Figure S12A). Additionally, higher levels of pAKT and pPCK1 were associated with shorter overall survival in patients with ICC (Supplementary Figure S12B-D).

Additionally, PROGENy [50] and Compass [51] were used to assess the activity of the PI3K pathway and its relationship with MVA pathway-related metabolic pathways in 41,419 ICC cells from 47 patients by integrating 3 public ICC scRNA sequencing dataset [46–48] (Figure 8E). A comparison of the metabolic activity between the top and bottom thirds of ICC cells based on PI3K-AKT activity revealed that PI3K-AKT-high ICC cells had a higher MVA pathway activity (Figure 8F, Supplementary Figure S12E). Moreover, HPLC-MS analysis verified that CCA cell lines or ICC-PDOs with higher levels of pAKT-pPCK1 had higher levels of MVA and CoQ<sub>10</sub>H<sub>2</sub>/CoQ<sub>10</sub> (Figure 8G). In summary, these findings revealed the important role of the pAKT-pPCK1 axis in the clinical progression of human ICC, supporting its potential for guiding clinical practice.

## 4 | DISCUSSION

In this study, we found that in AKT-hyperactivated ICC cells, PCK1 phosphorylation by AKT was observed to induce a functional shift from gluconeogenesis enzyme to protein kinase. This post-translational modification enabled pPCK1 to bind and phosphorylate LDHA, which correlated with elevated glycolytic flux. Concomitantly, these AKT-high ICC cells displayed selective ferroptosis resistance, resisting GPX4-GSH-targeting agents while remaining sensitive to FSP1-CoQ<sub>10</sub>H<sub>2</sub> pathway inhibitors. Further analysis revealed that pPCK1-LDHA interaction promoted SPRING lactylation at K82, a modification associated with enhanced MVA pathway activity. This

tumor general overview (C), tumor weight (D), tumor volume (E), intratumoral MDA concentrations for lipid peroxidation evaluation (F), flow cytometry analysis of CD3<sup>+</sup>CD8<sup>+</sup> T cell percentages (G) and TNF $\alpha$ <sup>+</sup>/IFN $\gamma$ <sup>+</sup> CD8<sup>+</sup> T cell percentages (H), and IHC analysis for CD8<sup>+</sup> T cell infiltration (I). (J-N) Similar in vivo setup as (C-I) with post-treatment (Placebo, CIT, Simv, CIT + Simv, CIT + Simv + MVA-Li) analyses including tumor general overview (J), tumor weight (K), tumor volume (L), intratumoral MDA concentrations for lipid peroxidation evaluation (M), and IHC analysis for CD8<sup>+</sup> T cell infiltration (N). For IHC analysis, 9 field of view were randomly selected from 5 slides corresponding to 5 mice in each group for statistical analysis. All data are mean  $\pm$  SD. Statistical significance was determined using 2-way ANOVA for multiple group comparisons and unpaired 2-tailed t-tests for comparisons between 2 groups. \*  $P < 0.05$ ; \*\*  $P < 0.01$ ; \*\*\*  $P < 0.001$ ; ns, not significant.

Abbreviations: ACAT2, acetyl-CoA acetyltransferase 2; HMGCS1, 3-hydroxy-3-methylglutaryl-CoA synthase 1; HMGCR, 3-hydroxy-3-methylglutaryl-CoA reductase; MVK, mevalonate kinase; MVD, mevalonate diphosphate decarboxylase; IDI1, isopentenyl-diphosphate delta isomerase 1; FDPS, farnesyl diphosphate synthase; FDFT1, farnesyl-diphosphate farnesyltransferase 1; SQLE, squalene epoxidase; LSS, lanosterol synthase; CYP51A1, cytochrome P450 family 51 subfamily A member 1; SC4MOL, sterol-C4-methyl oxidase-like; NSDHL, NAD(P)H steroid dehydrogenase-like; DHCR7, 7-dehydrocholesterol reductase; DHCR24, 24-dehydrocholesterol reductase; SPRING, SREBP regulating gene protein; Nala, sodium L-lactate; MVA-Li, mevalonic acid lithium salt; PPB, PCK1 phosphorylation blocker; Simv, Simvastatin; CIT, chemo-immunotherapy; MDA, malondialdehyde.

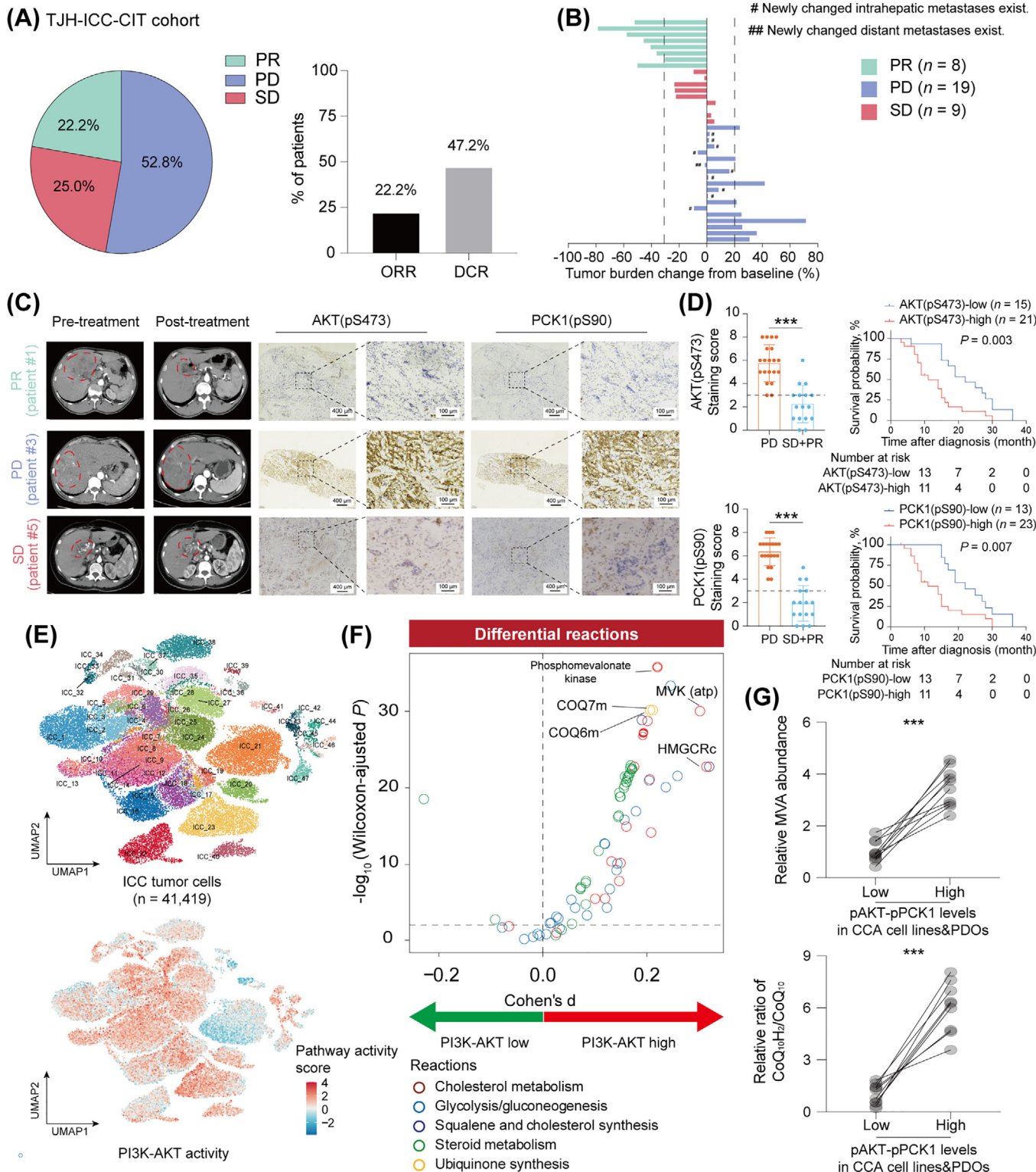


**FIGURE 8** Prognostic relevance of the pPCK1 in AKT-hyperactivated ICC patients undergoing CIT. (A) Clinical outcomes for 36 resectable ICC patients receiving durvalumab (anti-PD-L1 antibody) combined with cisplatin and gemcitabine (TJ-ICC-CIT cohort). (B) Best percentage change from baseline in tumor burden per patient according to modified RECIST (mRECIST 1.1) criteria. (C) IHC assessment of AKT (pS473) and PCK1 (pSer90) in samples from TJ-ICC-CIT cohort, with radiographic images (CT scans) and corresponding IHC data for 3 representative patients with PR/PD/SD. (D) Quantitative IHC analysis comparing AKT (pS473) and PCK1 (pS90) expression levels between PD and SD+PR patients. Kaplan-Meier analysis illustrates OS stratified by high (staining scores 4-8) versus low (staining scores 0-3) expression levels of AKT (pS473) and PCK1 (pS90). (E) UMAP plot of ICC tumor cells colored by patient (top) and PI3K-AKT activity

metabolic rewiring coincided with increased production of radical-trapping antioxidants (CoQ<sub>10</sub>H<sub>2</sub> and MK4), which paralleled the observed resistance to both ferroptosis and CIT regimens. Critically, pharmacological inhibition of the MVA pathway using simvastatin reduced CoQ<sub>10</sub>H<sub>2</sub>/MK4 levels and reversed resistance phenotype to CIT. Finally, ICC patients with elevated pAKT-pPCK1 axis activity showed diminished responses to CIT, suggesting a potential association between this axis and therapeutic outcomes.

Previous studies have demonstrated the diverse roles of AKT signaling in ferroptosis regulation. TRPML1-mediated ferroptosis suppression is essential for AKT-driven tumorigenesis and therapeutic resistance [72]. Hyperactive PI3K-AKT-mTOR signaling protects cancer cells from ferroptosis through SREBP1/SCD1-mediated lipogenesis [11]. Similarly, Tu et al. [73] demonstrated that the activation of the PI3K/AKT/mTOR signaling pathway upregulates HIF1 $\alpha$  and ABCD1 expression, thereby reducing lipid peroxidation and ferroptosis. These findings highlight the context-specific mechanisms of AKT-mediated ferroptosis resistance across cancer types.

Our findings identified pPCK1, a phosphorylated form of PCK1, as the primary mediator of ferroptosis resistance in AKT-hyperactivated ICC. Song et al. [74] previously identified PCK1 as one of the top 3 ferroptosis resistance-associated enzymes in AKT-hyperactivated PANC1 cells. Tumor-repopulating cells (TRCs) exhibited strong ferroptosis resistance [75], PCK2 downregulation, and PCK1 upregulation [57]. Although these findings implicated PCK1 in ferroptosis regulation, the underlying mechanisms remain unclear. In this study, we demonstrated that pPCK1, driven by AKT hyperactivation, facilitates ferroptosis resistance through its pro-glycolytic and subsequent pro-lipogenic effects in ICC.

Mechanistically, pPCK1 interacted with LDHA and phosphorylates it, thereby enhancing glycolytic activity and lactate production. Increased lactate production enhanced KAT7-mediated lactylation of SPRING at K82, which subsequently activated the SREBP2-driven MVA

pathway. This pathway facilitated ferroptosis resistance by enhancing ICC cell reliance on the FSP1-CoQ<sub>10</sub>H<sub>2</sub> system. Lipidomic analysis revealed no significant increase in the MUFA/PUFA ratio that is typically regulated by the SREBP1-SCD1 axis. Instead, targeted metabolic analyses demonstrated increased levels of MVA pathway metabolites, including MVA, CoQ<sub>10</sub>H<sub>2</sub>, and MK4, highlighting a different lipogenic mechanism in AKT-hyperactivated ICC.

Our findings were consistent with those of previous studies that have assessed PCK1 in cancer. Xu et al. [40] observed that pPCK1 loses its gluconeogenic function, whereas Li et al. [57] demonstrated that PCK1 upregulation enhanced glycolysis in TRCs. Shi et al. [76] reported that PCK1 acted as a tumor suppressor in clear cell renal cell carcinoma by destabilizing LDHA and thereby inhibiting tumor growth. However, in ICC, the interaction between PCK1 and LDHA was not a tumor-suppressive event, nor does their binding lead to a decrease in LDHA stability. In summary, these studies highlight the context-dependent dual roles of PCK1, which can act as either a tumor suppressor or oncogenic driver based on the cellular environment and metabolic state. Our study revealed a novel mechanism by which pPCK1 directly phosphorylates LDHA to enhance glycolysis and drive ferroptosis resistance through MVA pathway activation.

Clinically, our findings provided a potential strategy to overcome CIT resistance in AKT-hyperactivated ICC. Statins—that inhibited HMGR and target the MVA pathway—have demonstrated promise in reducing the risk of biliary tract cancers.

Cheung et al. [77] reported a lower incidence of CCA in statin users, whereas Wijarnpreecha et al. [78] identified a significant inverse association between statin use and CCA risk. Although these studies did not specifically assess the effect of statins on CIT efficacy, they provided a strong rationale for their safe use in patients with ICC. Our results indicated that targeting the pPCK1-pLDHA-SPRING-lac-MVA axis with statins may sensitize AKT-hyperactivated ICC cells to ferroptosis and enhance CIT responses.

(bottom). The scRNA sequencing data of ICC tumor cells ( $n = 41,419$ , from 47 ICC patients) were collected from public datasets, and the PI3K-AKT activity of ICC tumor cells was evaluated by PROGENy. (F) MVA pathway activation-related scores were generated using Compass, and differential activity between PI3K-AKT-high and PI3K-AKT-low ICC tumor cells was analyzed. (G) CCA cell lines ( $n = 10$ ) and ICC-PDOs ( $n = 10$ ) with varying levels of pAKT-pPCK1 were classified into pAKT-pPCK1 high and low groups, followed by quantitative analysis of MVA levels and the CoQ<sub>10</sub>H<sub>2</sub>/CoQ<sub>10</sub> ratio. All data are mean  $\pm$  SD. Statistical significance was determined using 2-way ANOVA for multiple group comparisons and unpaired 2-tailed t-tests for comparisons between 2 groups. \*  $P < 0.05$ ; \*\*  $P < 0.01$ ; \*\*\*  $P < 0.001$ ; ns, not significant. Abbreviations: ORR, overall response rate; DCR, disease control rate; PR, partial response; SD, stable disease; PD, progressive disease; OS, overall survival; IHC, immunohistochemistry; CT, computed tomography; mRECIST 1.1, modified response evaluation criteria in solid tumors version 1.1; ICC, intrahepatic cholangiocarcinoma; PI3K-AKT, phosphoinositide 3-kinase-protein kinase B pathway; CoQ<sub>10</sub>H<sub>2</sub>, reduced coenzyme Q10 (Ubiquinol); CoQ<sub>10</sub>, coenzyme Q10 (Ubiquinone); UMAP, uniform manifold approximation and projection; scRNA, single-cell RNA sequencing.

The study primarily relied on preclinical models. Although the findings regarding the role of the pAKT-pPCK1 axis in mediating ferroptosis resistance and CIT resistance, as well as the potential efficacy of simvastatin in CIT sensitization, are promising, they require validation in larger clinical cohorts and prospective clinical trials. Additionally, the mechanisms underlying CIT response variability in ICC subgroups beyond AKT hyperactivation remained to be further investigated. Finally, the sample size for clinical analysis was not determined a priori through power analysis, which may impact the robustness of the statistical conclusions.

## 5 | CONCLUSIONS

In conclusion, this study identified the pAKT-pPCK1-pLDHA-SPRINGlac axis as a novel driver of ferroptosis resistance in AKT-hyperactivated ICC. This pathway enhanced cellular dependence on the FSP1-CoQ<sub>10</sub>H<sub>2</sub> system by associating glycolytic activation with the MVA pathway upregulation, thereby facilitating ferroptosis and CIT resistance. Our findings established pPCK1 as a potential biomarker for identifying patients with ICC at risk of treatment resistance and provided a rationale for targeting the MVA pathway, such as through statin-based therapies, to enhance clinical outcomes.

### AUTHOR CONTRIBUTIONS

Wanguang Zhang, Jinghan Zhu, and Zeyang Ding designed the study and oversaw the research process. Jinghan Zhu and Yixiao Xiong performed the key experiments. Yuxin Zhang and Huifang Liang collected and analyzed clinical samples, performed public data analysis, provided clinical samples, and supported cell line and animal experiments. Kun Cheng contributed to the collection of clinical samples and the construction of patient-derived organoids. Yuanxiang Lu analyzed clinical samples and supported animal and immunoprecipitation experiments. Guangzhen Cai contributed to bioinformatics analysis. Yunhui Fan and Yang Wu assisted with cell line and animal experiments. Jinghan Zhu, Yixiao Xiong, and Yuxin Zhang drafted the initial manuscript. Hong Zhu, Zeyang Ding, and Huifang Liang revised the manuscript. Hong Zhu provided technical support for cell and animal model construction. Wanguang Zhang, Hong Zhu, Xiaoping Chen, Yixiao Xiong and Yuxin Zhang provided financial support. Wanguang Zhang and Xiaoping Chen ensured sufficient resources to complete the research and managed the overall administrative aspects of the project. All authors reviewed and approved the final version of the manuscript.

### AFFILIATIONS

<sup>1</sup>Hepatic Surgery Center, Tongji Hospital, Tongji Medical College, Huazhong University of Science and Technology, Wuhan, Hubei, P. R. China

<sup>2</sup>Hubei Key Laboratory of Hepato-Pancreato-Biliary Diseases, Wuhan, Hubei, P. R. China

<sup>3</sup>Department of Dermatology, Tongji Hospital, Tongji Medical College, Huazhong University of Science and Technology, Wuhan, Hubei, P. R. China

<sup>4</sup>Department of Gynecological Oncology, National Clinical Research Center for Obstetrics and Gynecology, Tongji Hospital, Tongji Medical College, Huazhong University of Science and Technology, Wuhan, Hubei, P. R. China

<sup>5</sup>Key Laboratory of Organ Transplantation, Ministry of Education, National Health Commission Key Laboratory of Organ Transplantation, Key Laboratory of Organ Transplantation, Chinese Academy of Medical Sciences, Wuhan, Hubei, P. R. China

<sup>6</sup>Department of Medical Oncology, the First Affiliated Hospital of Soochow University, Suzhou, Jiangsu, P. R. China

### ACKNOWLEDGEMENTS

We thank Prof. Weimin Wang (Huazhong University of Science and Technology) for guidance on study design and manuscript development, Prof. Bo Zhong (Wuhan University) for the Kras<sup>G12D</sup>/Tp53<sup>flox/flox</sup> mice, Prof. Hongyang Wang, Prof. Liwei Dong (Naval Medical University), Prof. Zhimin Lv, Prof. Daqian Xu (Zhejiang University), Prof. Chundong Yu, and Prof. Han You (Xiamen University) for cholangiocarcinoma cell lines and plasmid support, Dr. Hengyi Yu (Huazhong University of Science and Technology) for HPLC/MS expertise, and Dr. Jingjiao Song (Huazhong University of Science and Technology) of the Clinical Laboratory Medicine Research Center, Tongji Hospital for flow cytometry support. This study was funded by the National Natural Science Foundation of China (No. 81874149, 82303832, 82171834, 82403618), Knowledge Innovation Program of Wuhan-Shuguang Project (No. 2022020801020456), Key Research and Development Program of Social Development of Jiangsu Province (No. BE2022725), the Suzhou Science and Technology Development Plan Project (No. SKY2023049), the China Postdoctoral Science Foundation (No. 2024M761039), China National Postdoctoral Program for Innovative Talents (No. BX20240129), Postdoctor Project of Hubei Province (No. 2024HBBHCXA035), and Jiangsu Province Seventh 333 High Level (Second Level) Talents Project.

### CONFLICT OF INTEREST STATEMENT

The authors declare no potential conflicts of interest.

### ETHICS APPROVAL AND CONSENT TO PARTICIPATE

This study was approved by the Ethics Committee of Tongji Hospital (TJ-IRB20230112). Informed consent was

obtained from patients or their legal guardians. Animal studies were conducted in accordance with the guidelines approved by the Institutional Animal Care and Use Committee of Tongji Hospital, Huazhong University of Science and Technology (TJH-202109004).

#### DATA AVAILABILITY STATEMENT

CRISPR/Cas9 screen data has been deposited in National Genomics Data Center (PRJCA020671); IP-MS data has been deposited in iProX (IPX0007371000). Additional data supporting this study are available from corresponding authors upon reasonable request.

#### ORCID

Jinghan Zhu  <https://orcid.org/0000-0002-6310-1672>

Huifang Liang  <https://orcid.org/0000-0001-6874-3634>

Wanguang Zhang  <https://orcid.org/0000-0003-3184-9907>

#### REFERENCES

- Rizvi S, Khan SA, Hallemeier CL, Kelley RK, Gores GJ. Cholangiocarcinoma - evolving concepts and therapeutic strategies. *Nat Rev Clin Oncol*. 2018;15(2):95-111.
- Rauth S, Malafa M, Ponnusamy MP, Batra SK. Emerging Trends in Gastrointestinal Cancer Targeted Therapies: Harnessing Tumor Microenvironment, Immune Factors, and Metabolomics Insights. *Gastroenterology*. 2024;167(5):867-84.
- Oh D-Y, Ruth He A, Qin S, Chen L-T, Okusaka T, Vogel A, et al. Durvalumab plus gemcitabine and cisplatin in advanced biliary tract cancer. *NEJM Evid*. 2022;1(8):EVIDoa2200015.
- Satriano L, Lewinska M, Rodrigues PM, Banales JM, Andersen JB. Metabolic rearrangements in primary liver cancers: cause and consequences. *Nat Rev Gastroenterol Hepatol*. 2019;16(12):748-66.
- Wang Y, Zheng L, Shang W, Yang Z, Li T, Liu F, et al. Wnt/beta-catenin signaling confers ferroptosis resistance by targeting GPX4 in gastric cancer. *Cell Death Differ*. 2022;29(11):2190-202.
- Chen Y, Li L, Lan J, Cui Y, Rao X, Zhao J, et al. CRISPR screens uncover protective effect of PTK as a regulator of chemotherapy-induced ferroptosis in hepatocellular carcinoma. *Mol Cancer*. 2022;21(1):11.
- Wang W, Green M, Choi JE, Gijon M, Kennedy PD, Johnson JK, et al. CD8(+) T cells regulate tumour ferroptosis during cancer immunotherapy. *Nature*. 2019;569(7755):270-4.
- Hänggi K, Ruffell B. Cell death, therapeutics, and the immune response in cancer. *Trends Cancer*. 2023;9(5):381-96.
- Doll S, Proneth B, Tyurina YY, Panzilius E, Kobayashi S, Ingold I, et al. ACSL4 dictates ferroptosis sensitivity by shaping cellular lipid composition. *Nat Chem Biol*. 2017;13(1):91-8.
- Liao P, Wang W, Wang W, Kryczek I, Li X, Bian Y, et al. CD8(+) T cells and fatty acids orchestrate tumor ferroptosis and immunity via ACSL4. *Cancer Cell*. 2022;40(4):365-78.e6.
- Yi J, Zhu J, Wu J, Thompson CB, Jiang X. Oncogenic activation of PI3K-AKT-mTOR signaling suppresses ferroptosis via SREBP-mediated lipogenesis. *Proc Natl Acad Sci U S A*. 2020;117(49):31189-97.
- Hong X, Roh W, Sullivan RJ, Wong KHK, Wittner BS, Guo H, et al. The Lipogenic Regulator SREBP2 Induces Transferrin in Circulating Melanoma Cells and Suppresses Ferroptosis. *Cancer Discov*. 2021;11(3):678-95.
- Liang D, Minikes AM, Jiang X. Ferroptosis at the intersection of lipid metabolism and cellular signaling. *Mol Cell*. 2022;82(12):2215-27.
- Hill MA, Alexander WB, Guo B, Kato Y, Patra K, O'Dell MR, et al. Kras and Tp53 Mutations Cause Cholangiocyte- and Hepatocyte-Derived Cholangiocarcinoma. *Cancer Res*. 2018;78(16):4445-51.
- Wang W, Yuan T, Ma L, Zhu Y, Bao J, Zhao X, et al. Hepatobiliary Tumor Organoids Reveal HLA Class I Neoantigen Landscape and Antitumoral Activity of Neoantigen Peptide Enhanced with Immune Checkpoint Inhibitors. *Adv Sci (Weinh)*. 2022;9(22):2105810.
- Tomlinson JL, Li B, Yang J, Loeuillard E, Stumpf HE, Kuipers H, et al. Syngeneic murine models with distinct immune microenvironments represent subsets of human intrahepatic cholangiocarcinoma. *J Hepatol*. 2024;80(6):892-903.
- Dobin A, Davis CA, Schlesinger F, Drenkow J, Zaleski C, Jha S, et al. STAR: ultrafast universal RNA-seq aligner. *Bioinformatics*. 2013;29(1):15-21.
- Liao Y, Smyth GK, Shi W. The R package Rsubread is easier, faster, cheaper and better for alignment and quantification of RNA sequencing reads. *Nucleic Acids Res*. 2019;47(8):e47.
- Ritchie ME, Phipson B, Wu D, Hu Y, Law CW, Shi W, et al. limma powers differential expression analyses for RNA-sequencing and microarray studies. *Nucleic Acids Res*. 2015;43(7):e47.
- Leek JT, Johnson WE, Parker HS, Jaffe AE, Storey JD. The sva package for removing batch effects and other unwanted variation in high-throughput experiments. *Bioinformatics*. 2012;28(6):882-3.
- Zhu XG, Chudnovskiy A, Baudrier L, Prizer B, Liu Y, Ostendorf BN, et al. Functional Genomics In Vivo Reveal Metabolic Dependencies of Pancreatic Cancer Cells. *Cell Metab*. 2021;33(1):211-21.e6.
- Wang X, Tokheim C, Gu SS, Wang B, Tang Q, Li Y, et al. In vivo CRISPR screens identify the E3 ligase Cop1 as a modulator of macrophage infiltration and cancer immunotherapy target. *Cell*. 2021;184(21):5357-74.e22.
- Li W, Xu H, Xiao T, Cong L, Love MI, Zhang F, et al. MAGeCK enables robust identification of essential genes from genome-scale CRISPR/Cas9 knockout screens. *Genome Biol*. 2014;15(12):554.
- Percie du Sert N, Hurst V, Ahluwalia A, Alam S, Avey MT, Baker M, et al. The ARRIVE guidelines 2.0: Updated guidelines for reporting animal research. *PLoS Biol*. 2020;18(7):e3000410.
- National Research Council Committee for the Update of the Guide for the Care and Use of Laboratory Animals. *The National Academies Collection: Reports funded by National Institutes of Health. Guide for the Care and Use of Laboratory Animals*. Washington (DC): National Academies Press (US) Copyright © 2011, National Academy of Sciences; 2011.
- Liu F, Liao Z, Qin L, Zhang Z, Zhang Q, Han S, et al. Targeting VPS72 inhibits ACTL6A/MYC axis activity in HCC progression. *Hepatology*. 2023;78(5):1384-401.

27. Liu Y, Fang Y, Chen X, Wang Z, Liang X, Zhang T, et al. Gasdermin E-mediated target cell pyroptosis by CAR T cells triggers cytokine release syndrome. *Sci Immunol.* 2020;5(43):eaax7969.
28. Xiong YX, Zhang XC, Zhu JH, Zhang YX, Pan YL, Wu Y, et al. Collagen I-DDR1 signaling promotes hepatocellular carcinoma cell stemness via Hippo signaling repression. *Cell Death Differ.* 2023;30(7):1648-65.
29. Doman JL, Sousa AA, Randolph PB, Chen PJ, Liu DR. Designing and executing prime editing experiments in mammalian cells. *Nat Protoc.* 2022;17(11):2431-68.
30. Hsu JY, Grünewald J, Szalay R, Shih J, Anzalone AV, Lam KC, et al. PrimeDesign software for rapid and simplified design of prime editing guide RNAs. *Nat Commun.* 2021;12(1):1034.
31. Kelstrup CD, Bekker-Jensen DB, Arrey TN, Hogrebe A, Harder A, Olsen JV. Performance Evaluation of the Q Exactive HF-X for Shotgun Proteomics. *J Proteome Res.* 2018;17(1):727-38.
32. Cox J, Mann M. MaxQuant enables high peptide identification rates, individualized p.p.b.-range mass accuracies and proteome-wide protein quantification. *Nat Biotechnol.* 2008;26(12):1367-72.
33. Cox J, Hein MY, Luber CA, Paron I, Nagaraj N, Mann M. Accurate proteome-wide label-free quantification by delayed normalization and maximal peptide ratio extraction, termed MaxLFQ. *Mol Cell Proteomics.* 2014;13(9):2513-26.
34. UniProt: the universal protein knowledgebase in 2021. *Nucleic Acids Res.* 2021;49(D1):D480-9.
35. Song JW, Lam SM, Fan X, Cao WJ, Wang SY, Tian H, et al. Omics-Driven Systems Interrogation of Metabolic Dysregulation in COVID-19 Pathogenesis. *Cell Metab.* 2020;32(2):188-202.e5.
36. Lam SM, Zhang C, Wang Z, Ni Z, Zhang S, Yang S, et al. A multi-omics investigation of the composition and function of extracellular vesicles along the temporal trajectory of COVID-19. *Nat Metab.* 2021;3(7):909-22.
37. Claessens AJ, Yeung CK, Risler LJ, Phillips BR, Himmelfarb J, Shen DD. Rapid and sensitive analysis of reduced and oxidized coenzyme Q10 in human plasma by ultra performance liquid chromatography-tandem mass spectrometry and application to studies in healthy human subjects. *Ann Clin Biochem.* 2016;53(Pt 2):265-73.
38. Usui Y, Nishimura N, Kobayashi N, Okanou T, Kimoto M, Ozawa K. Measurement of vitamin K in human liver by gradient elution high-performance liquid chromatography using platinum-black catalyst reduction and fluorimetric detection. *J Chromatogr.* 1989;489(2):291-301.
39. Jemal M, Schuster A, Whigan DB. Liquid chromatography/tandem mass spectrometry methods for quantitation of mevalonic acid in human plasma and urine: method validation, demonstration of using a surrogate analyte, and demonstration of unacceptable matrix effect in spite of use of a stable isotope analog internal standard. *Rapid Commun Mass Spectrom.* 2003;17(15):1723-34.
40. Xu D, Wang Z, Xia Y, Shao F, Xia W, Wei Y, et al. The gluconeogenic enzyme PCK1 phosphorylates INSIG1/2 for lipogenesis. *Nature.* 2020;580(7804):530-5.
41. Ye B, Liu B, Hao L, Zhu X, Yang L, Wang S, et al. Klf4 glutamylation is required for cell reprogramming and early embryonic development in mice. *Nat Commun.* 2018;9(1):1261.
42. Obenaus JC, Cantley LC, Yaffe MB. Scansite 2.0: Proteome-wide prediction of cell signaling interactions using short sequence motifs. *Nucleic Acids Res.* 2003;31(13):3635-41.
43. Hornbeck PV, Zhang B, Murray B, Kornhauser JM, Latham V, Skrzypek E. PhosphoSitePlus, 2014: mutations, PTMs and recalibrations. *Nucleic Acids Res.* 2015;43(Database issue):D512-20.
44. Cho KF, Branon TC, Udeshi ND, Myers SA, Carr SA, Ting AY. Proximity labeling in mammalian cells with TurboID and split-TurboID. *Nat Protoc.* 2020;15(12):3971-99.
45. Li X, Jiang Y, Meisenhelder J, Yang W, Hawke DH, Zheng Y, et al. Mitochondria-Translocated PGK1 Functions as a Protein Kinase to Coordinate Glycolysis and the TCA Cycle in Tumorigenesis. *Mol Cell.* 2016;61(5):705-19.
46. Xue R, Zhang Q, Cao Q, Kong R, Xiang X, Liu H, et al. Liver tumour immune microenvironment subtypes and neutrophil heterogeneity. *Nature.* 2022;612(7938):141-7.
47. Ma L, Hernandez MO, Zhao Y, Mehta M, Tran B, Kelly M, et al. Tumor Cell Biodiversity Drives Microenvironmental Reprogramming in Liver Cancer. *Cancer Cell.* 2019;36(4):418-30.e6.
48. Zhang M, Yang H, Wan L, Wang Z, Wang H, Ge C, et al. Single-cell transcriptomic architecture and intercellular crosstalk of human intrahepatic cholangiocarcinoma. *J Hepatol.* 2020;73(5):1118-30.
49. Yang C, Geng H, Yang X, Ji S, Liu Z, Feng H, et al. Targeting the immune privilege of tumor-initiating cells to enhance cancer immunotherapy. *Cancer Cell.* 2024;42(12):2064-81.e19.
50. Schubert M, Klinger B, Klünemann M, Sieber A, Uhlitz F, Sauer S, et al. Perturbation-response genes reveal signaling footprints in cancer gene expression. *Nat Commun.* 2018;9(1):20.
51. Wagner A, Wang C, Fessler J, DeTomaso D, Avila-Pacheco J, Kaminski J, et al. Metabolic modeling of single Th17 cells reveals regulators of autoimmunity. *Cell.* 2021;184(16):4168-85.e21.
52. Fu L, Li S, Xiao W, Yu K, Li S, Yuan S, et al. DGKA Mediates Resistance to PD-1 Blockade. *Cancer Immunol Res.* 2021;9(4):371-85.
53. Li J, Pan C, Boese AC, Kang J, Umamo AD, Magliocca KR, et al. DGKA Provides Platinum Resistance in Ovarian Cancer Through Activation of c-JUN-WEE1 Signaling. *Clin Cancer Res.* 2020;26(14):3843-55.
54. Liu J, Wei Y, Wu Y, Li J, Sun J, Ren G, et al. ATP2C2 Has Potential to Define Tumor Microenvironment in Breast Cancer. *Front Immunol.* 2021;12:657950.
55. Huang D, Wang Y, Thompson JW, Yin T, Alexander PB, Qin D, et al. Cancer-cell-derived GABA promotes  $\beta$ -catenin-mediated tumour growth and immunosuppression. *Nat Cell Biol.* 2022;24(2):230-41.
56. Ma R, Zhang W, Tang K, Zhang H, Zhang Y, Li D, et al. Switch of glycolysis to gluconeogenesis by dexamethasone for treatment of hepatocarcinoma. *Nat Commun.* 2013;4:2508.
57. Li Y, Luo S, Ma R, Liu J, Xu P, Zhang H, et al. Upregulation of cytosolic phosphoenolpyruvate carboxykinase is a critical metabolic event in melanoma cells that repopulate tumors. *Cancer Res.* 2015;75(7):1191-6.
58. Tang K, Zhu L, Chen J, Wang D, Zeng L, Chen C, et al. Hypoxia Promotes Breast Cancer Cell Growth by Activating a Glycogen Metabolic Program. *Cancer Res.* 2021;81(19):4949-63.
59. Gou D, Liu R, Shan X, Deng H, Chen C, Xiang J, et al. Gluconeogenic enzyme PCK1 supports S-adenosylmethionine biosyn-

- thesis and promotes H3K9me3 modification to suppress hepatocellular carcinoma progression. *J Clin Invest.* 2023;133(13).
60. Montal ED, Dewi R, Bhalla K, Ou L, Hwang BJ, Ropell AE, et al. PEPCK Coordinates the Regulation of Central Carbon Metabolism to Promote Cancer Cell Growth. *Mol Cell.* 2015;60(4):571-83.
  61. Gaschler MM, Andia AA, Liu H, Csuka JM, Hurlocker B, Vaiana CA, et al. FINO(2) initiates ferroptosis through GPX4 inactivation and iron oxidation. *Nat Chem Biol.* 2018;14(5):507-15.
  62. Bian X, Jiang H, Meng Y, Li YP, Fang J, Lu Z. Regulation of gene expression by glycolytic and gluconeogenic enzymes. *Trends Cell Biol.* 2022;32(9):786-99.
  63. Yang X, Wang Z, Zandkarimi F, Liu Y, Duan S, Li Z, et al. Regulation of VKORC1L1 is critical for p53-mediated tumor suppression through vitamin K metabolism. *Cell Metab.* 2023;35(8):1474-90.e8.
  64. Gao R, Li Y, Xu Z, Zhang F, Xu J, Hu Y, et al. Mitochondrial pyruvate carrier 1 regulates fatty acid synthase lactylation and mediates treatment of nonalcoholic fatty liver disease. *Hepatology.* 2023; 78(6):1800-15.
  65. Chen Y, Wu J, Zhai L, Zhang T, Yin H, Gao H, et al. Metabolic regulation of homologous recombination repair by MRE11 lactylation. *Cell.* 2024;187(2):294-311.e21.
  66. Chen H, Li Y, Li H, Chen X, Fu H, Mao D, et al. NBS1 lactylation is required for efficient DNA repair and chemotherapy resistance. *Nature.* 2024;631(8021):663-9.
  67. Hendrix S, Kingma J, Ottenhoff R, Valiloo M, Svecla M, Zijlstra LF, et al. Hepatic SREBP signaling requires SPRING to govern systemic lipid metabolism in mice and humans. *Nat Commun.* 2023;14(1):5181.
  68. Loregger A, Raaben M, Nieuwenhuis J, Tan JME, Jae LT, van den Hengel LG, et al. Haploid genetic screens identify SPRING/C12ORF49 as a determinant of SREBP signaling and cholesterol metabolism. *Nat Commun.* 2020;11(1):1128.
  69. Bayraktar EC, La K, Karpman K, Unlu G, Ozerdem C, Ritter DJ, et al. Metabolic coessentiality mapping identifies C12orf49 as a regulator of SREBP processing and cholesterol metabolism. *Nat Metab.* 2020;2(6):487-98.
  70. Aregger M, Lawson KA, Billmann M, Costanzo M, Tong AHY, Chan K, et al. Systematic mapping of genetic interactions for de novo fatty acid synthesis identifies C12orf49 as a regulator of lipid metabolism. *Nat Metab.* 2020;2(6):499-513.
  71. Goldstein JL, Brown MS. Regulation of the mevalonate pathway. *Nature.* 1990;343(6257):425-30.
  72. Zhang HL, Hu BX, Ye ZP, Li ZL, Liu S, Zhong WQ, et al. TRPML1 triggers ferroptosis defense and is a potential therapeutic target in AKT-hyperactivated cancer. *Sci Transl Med.* 2024;16(753):eadk0330.
  73. Tu RH, Wu SZ, Huang ZN, Zhong Q, Ye YH, Zheng CH, et al. Neurotransmitter Receptor HTR2B Regulates Lipid Metabolism to Inhibit Ferroptosis in Gastric Cancer. *Cancer Res.* 2023;83(23):3868-85.
  74. Song X, Liu J, Kuang F, Chen X, Zeh HJ, 3rd, Kang R, et al. PDK4 dictates metabolic resistance to ferroptosis by suppressing pyruvate oxidation and fatty acid synthesis. *Cell Rep.* 2021;34(8):108767.
  75. Li Z, Xu ZM, Chen WP, Du XJ, Ou CX, Luo ZK, et al. Tumor-repopulating cells evade ferroptosis via PCK2-dependent phospholipid remodeling. *Nat Chem Biol.* 2024;20(10):1341-52.
  76. Shi L, An S, Liu Y, Liu J, Wang F. PCK1 Regulates Glycolysis and Tumor Progression in Clear Cell Renal Cell Carcinoma Through LDHA. *Oncotargets Ther.* 2020;13:2613-27.
  77. Cheung KS, Yeung YWM, Wong WS, Li B, Seto WK, Leung WK. Statins associate with lower risk of biliary tract cancers: A systematic review and meta-analysis. *Cancer Med.* 2023;12(1):557-68.
  78. Wijarnpreecha K, Aby ES, Ghaz H, Cheungpasitporn W, Lukens FJ, Harnois DM, et al. Statins and Risk of Cholangiocarcinoma: A Systematic Review and Meta-analysis. *J Gastrointest Liver Dis.* 2020;29(4):629-35.

## SUPPORTING INFORMATION

Additional supporting information can be found online in the Supporting Information section at the end of this article.

**How to cite this article:** Zhu J, Xiong Y, Zhang Y, Liang H, Cheng K, Lu Y, et al. Simvastatin overcomes the pPCK1-pLDHA-SPRINGlac axis-mediated ferroptosis and chemo-immunotherapy resistance in AKT-hyperactivated intrahepatic cholangiocarcinoma. *Cancer Commun.* 2025;1–34. <https://doi.org/10.1002/cac2.70036>